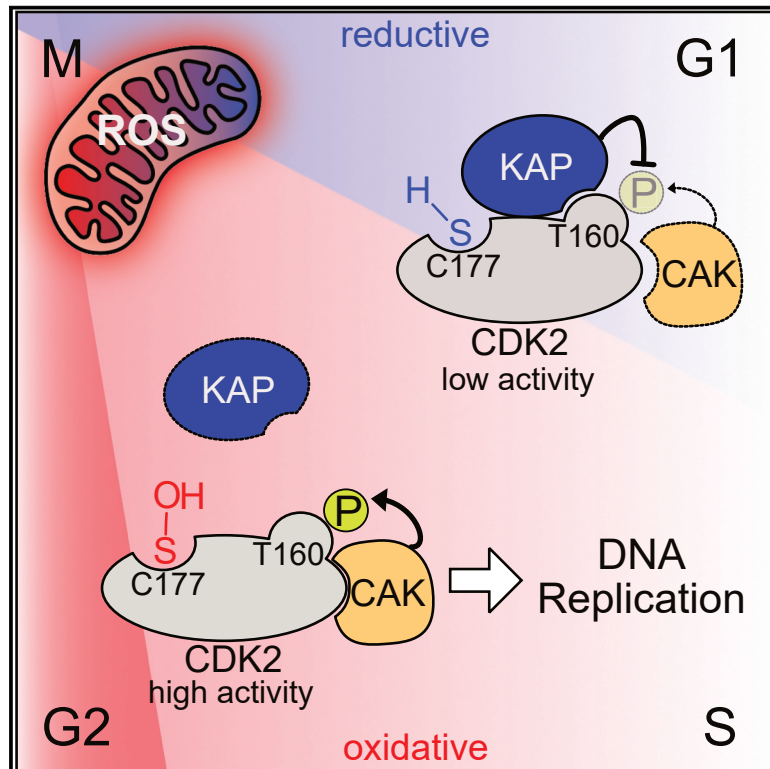


Developmental Cell

A ROS-dependent mechanism promotes CDK2 phosphorylation to drive progression through S phase

Graphical abstract



Authors

Dilyana Georgieva Kirova,
 Kristyna Judasova, Julia Vorhauser,
 Thomas Zerjatke, Jacky Kieran Leung,
 Ingmar Glauche, Jörg Mansfeld

Correspondence

jorg.mansfeld@icr.ac.uk

In brief

Reactive oxygen species (ROS) are by-products of mitochondrial respiration. Kirova et al. find that mitochondrial ROS increase during the cell cycle and oxidize cyclin-dependent kinase 2 (CDK2) to regulate its interaction with KAP phosphatase. CDK2 oxidation promotes T-loop phosphorylation and the CDK2 activity needed for DNA replication and proliferation.

Highlights

- Mitochondrial ROS drive cell cycle progression and proliferation
- Cyclin-dependent kinase 2 (CDK2) is increasingly oxidized during the cell cycle
- The oxidation state of a conserved cysteine on CDK2 regulates KAP binding
- CDK2 oxidation promotes T-loop phosphorylation and DNA replication

Article

A ROS-dependent mechanism promotes CDK2 phosphorylation to drive progression through S phase

Dilyana Georgieva Kirova,^{2,4} Kristyna Judasova,^{2,4} Julia Vorhauser,^{1,2} Thomas Zerjatke,³ Jacky Kieran Leung,¹ Ingmar Glauche,³ and Jörg Mansfeld^{1,2,5,*}

¹Division of Cancer Biology, The Institute of Cancer Research, London SW3 6JB, UK

²Cell Cycle, Biotechnology Center, Technische Universität Dresden, 01307 Dresden, Germany

³Institute for Medical Informatics and Biometry, Carl Gustav Carus Faculty of Medicine, Technische Universität Dresden, 01307 Dresden, Germany

⁴These authors contributed equally

⁵Lead contact

*Correspondence: jorg.mansfeld@icr.ac.uk

<https://doi.org/10.1016/j.devcel.2022.06.008>

SUMMARY

Reactive oxygen species (ROS) at the right concentration promote cell proliferation in cell culture, stem cells, and model organisms. However, the mystery of how ROS signaling is coordinated with cell cycle progression and integrated into the cell cycle control machinery on the molecular level remains unsolved. Here, we report increasing levels of mitochondrial ROS during the cell cycle in human cell lines that target cyclin-dependent kinase 2 (CDK2). Chemical and metabolic interferences with ROS production decrease T-loop phosphorylation on CDK2 and so impede its full activation and thus its efficient DNA replication. ROS regulate CDK2 activity through the oxidation of a conserved cysteine residue near the T-loop, which prevents the binding of the T-loop phosphatase KAP. Together, our data reveal how mitochondrial metabolism is coupled with DNA replication and cell cycle progression via ROS, thereby demonstrating how KAP activity toward CDKs can be cell cycle regulated.

INTRODUCTION

Reactive oxygen species (ROS) are oxygen-containing molecules with high chemical reactivity to “steal” electrons from molecules (oxidation). Excessive exposure to ROS during oxidative stress or from external sources such as ionizing agents can oxidize proteins, cause DNA mutations, and trigger lipid peroxidation (Schieber and Chandel, 2014). The major sources of intracellular ROS are superoxide anions ($O_2^{\cdot-}$) produced from membrane-associated NADPH oxidases (NOXs) and mitochondria, in response to growth factor (GF) signaling or as by-products of oxidative phosphorylation, respectively (Schieber and Chandel, 2014; Bedard and Krause, 2007; Murphy, 2009). $O_2^{\cdot-}$ molecules are subsequently converted to hydrogen peroxide (H_2O_2), either spontaneously or catalytically by superoxide dismutases (Möller et al., 2019; Wang et al., 2018). H_2O_2 is more stable, membrane-permeant, and at physiological concentrations can act as a signaling molecule in a variety of biological processes such as GF signaling, proliferation, differentiation, and adaptation to hypoxia (Holmström and Finkel, 2014; Reczek and Chandel, 2017; Shadel and Horvath, 2015). ROS signaling is in part mediated by reversible oxidation of cysteine thiols to sulfenic acids (R-SOH) and intra- or inter-molecular disulfide bonds,

which act as reversible posttranslational modifications (PTMs) that can regulate activity, localization, stability, and interactions of proteins (Reddie and Carroll, 2008).

Low levels of ROS, in particular of H_2O_2 , have been shown to promote proliferation of stem cells, differentiated cells, and cancer cells (Armstrong et al., 2010; Gurusamy et al., 2009; Adusumilli et al., 2021; Alfar et al., 2017; Moll et al., 2018; Sigaud et al., 2005; Safford et al., 1994; Irani et al., 1997; Ogrunc et al., 2014). Mechanistically, this proliferative effect is best understood for GF signaling, where NOX-derived H_2O_2 activates membrane-associated receptor tyrosine kinases while inhibiting counteracting phosphatases (Holmström and Finkel, 2014), so that sustained GF signaling can initiate transcriptional programs to promote the G0/G1 and G1/S transitions (Burhans and Heintz, 2009; Chiu and Dawes, 2012). Mitochondrial ROS can also activate transcriptional programs linked to proliferation (Owusu-Ansah et al., 2008; Weinberg et al., 2010; Tsai et al., 2011; Connor et al., 2005); however, whether or not ROS directly regulate the cell cycle independent of transcriptional signaling remains elusive.

A potential target of mitochondrial ROS could be the central regulatory cell cycle network mediated by cyclin-dependent kinases (CDKs). CDKs are activated by a conserved two-step

mechanism: binding of a cell cycle stage-specific cyclin and phosphorylation of a threonine residue (T160 in cyclin-dependent kinase 2 [CDK2]) within the activation segment of the kinase domain (T-loop) (Morgan, 2007). T-loop phosphorylation is carried out by a trimeric CDK-activating kinase (CAK, a complex of CDK7, cyclin H and MAT1) and opposed by CDK-associated phosphatase (KAP) and protein phosphatase 2C-like proteins (Fesquet et al., 1993; Poon et al., 1993; Solomon et al., 1993; Fisher and Morgan, 1994; Mäkelä et al., 1994; Poon and Hunter, 1995; Hannon et al., 1994; Gyuris et al., 1993; Cheng et al., 1999). Whether T-loop phosphorylation is regulated to ensure that the correct CDK becomes fully activated at the right time is still debated, since CAK is considered constitutively active (Fisher, 2005) and KAP activity regulation is unclear. Cell cycle stage and CDK specificity of T-loop phosphorylation, i.e., on CDK2 and CDK1, is in part achieved by preferential binding of CAK to monomeric CDK2 and cyclin-complexed CDK1, respectively (Larochelle et al., 2007; Merrick et al., 2008; Fisher and Morgan, 1994; Desai et al., 1995). Although KAP binds to both monomeric and cyclin-complexed CDKs (Poon and Hunter, 1995; Gyuris et al., 1993; Hannon et al., 1994), it can only dephosphorylate monomeric CDKs, i.e., once the bound cyclin is degraded (Poon and Hunter, 1995). This results in a conceptual problem for CDK2 activation during S phase, when cyclin E is degraded and CDK2 switches from cyclin E to cyclin A, meaning that T160 can be targeted by CAK and KAP at the same time.

Here, we employ retina pigment epithelial cells (RPE-1) as a non-transformed cell cycle model to monitor and interrogate intracellular ROS production along with cell cycle progression and CDK2 activation. We uncover that the levels of mitochondrial ROS increase in a cell cycle-dependent manner that recapitulates the activity of S phase regulator, CDK2. We show that oxidation of a cysteine that is conserved in CDK2 but not in other CDKs ensures T-loop phosphorylation required for efficient DNA replication and S phase progression. Our data reveal a regulatory mechanism for CDK2 activity via KAP that provides feedback from mitochondrial metabolism to cell cycle control and proliferation.

RESULTS

Proliferation and S phase progression require oxidative events

To investigate the interplay between physiological ROS signaling and cell cycle progression, we chose human telomerase reverse transcriptase (hTERT)-immortalized RPE-1 cells as a well-established model cell line with unperturbed cell cycle control (Bodnar et al., 1998). We first assessed whether RPE-1 cells require oxidative events for normal proliferation, as has been reported for other experimental models (Wartenberg et al., 1999; Havens et al., 2006; Murrell et al., 1990; Ohguro et al., 1999; Paul et al., 2014; Alfari et al., 2017). Indeed, treating RPE-1 cells with the antioxidant N-acetyl-L-cysteine (NAC) for 48 h reduced proliferation in a dose-dependent manner (Figure S1A). The decrease in proliferation was not due to induction of apoptosis as monitored by poly ADP-ribose polymerase (PARP) cleavage (Figure S1B). To determine the cell cycle stages sensitive to reducing conditions, we employed RPE-1 cells expressing three endogenous proteins tagged with different fluorescent proteins: (1) proliferating cell nuclear antigen (Ruby-PCNA) to detect replication

foci in S phase, (2) cyclin A2-Venus to distinguish cyclin A2-negative G1 cells from cyclin A2-positive S and G2 cells, and (3) histone 3.1-turquoise2 (H3.1-Turq2) to segment nuclei (Zerjatke et al., 2017). By assessing PCNA foci and cyclin A2 expression, we could classify cells as G1, S, or G2 phase based on snapshots (Figure S1C). This analysis revealed that the addition of NAC at all concentrations significantly increased the proportion of cells in S phase. We also observed that low (6 mM) concentrations of NAC reduced the number of cells in G1, whereas higher concentrations (8 and 10 mM) reduced the cells in G2 (Figure S1D). NAC is a general reductant and does not discriminate between different forms of ROS; therefore, we tested a membrane-permeant polyethylene glycol-linked catalase (PEG-CAT) to specifically target H₂O₂, which is considered to be the second messenger of ROS signaling (Winterbourn, 2008). Here, we combined Ruby-PCNA and H3.1-Turq2 with Fucci-Gem, a well-established anaphase promoting complex/cyclosome (APC/C) activity reporter that accumulates after the G1/S transition when APC/C is inactivated (Sakaue-Sawano et al., 2008). Fucci-Gem marks S and G2 phase cells which can be subsequently separated based on replication foci with Ruby-PCNA (Figure 1A). As with NAC, adding PEG-CAT strongly reduced cell proliferation (Figure 1B) and significantly increased the fraction of S phase at the expense of G1 (Figure 1C). To assess whether ROS directly promote RPE-1 cell proliferation, we increased the intracellular levels of ROS by using a genetically encoded D-amino acid oxidase (DAO) from *Rhodospiridium toruloides*, which converts medium-supplied D-alanine to a keto-acid, ammonia, and H₂O₂ (Lee and Chu, 1996; Figure 1D). The increase of H₂O₂ in response to D- but not L-alanine can be directly monitored by imaging of the ratio-metric H₂O₂ sensor HyPer2 fused to the N terminus of DAO (Figure 1E; Matlashov et al., 2014). DAO was further linked to a nuclear export sequence (NES, HyPer2-DAO-NES) to recapitulate mitochondrial ROS released through the outer mitochondrial membrane in the form of H₂O₂ (Shadel and Horvath, 2015). Indeed, the lowest concentration of D-alanine we applied (0.5 mM) significantly increased proliferation, whereas higher concentrations (2.5 or 5 mM) or addition of PEG-CAT had adverse effects (Figure 1F). Of note, the pro-proliferative effect of D-alanine at low concentrations and anti-proliferative effect at higher concentrations highlight the dual role of H₂O₂, which is dependent on dose and the antioxidant capacity of the cells (Gough and Cotter, 2011). These results suggest that oxidative events, mediated by H₂O₂, are required for normal proliferation of RPE-1 cells.

ROS levels increase during the cell cycle

We further investigated how physiological ROS production is correlated with cell cycle progression. We employed the ROS probe CellRox Deep Red to determine the overall ROS content in living cells that express Ruby-PCNA and cyclin A2-Venus to define the cell cycle phases. Compared with G1, cells in S and G2 phases showed increased labeling of CellRox Deep Red (Figure 2A). In agreement, flow cytometry analysis revealed significant increases in cellular ROS from G1 to S and S to G2/M phases indicative of ROS fluctuations during the cell cycle (Figure 2B). Notably, the ~25% increase of ROS from G1 to S phase is of the same magnitude as pro-proliferative ROS production by HyPer2-DAO-NES following 0.5 mM D-alanine treatment

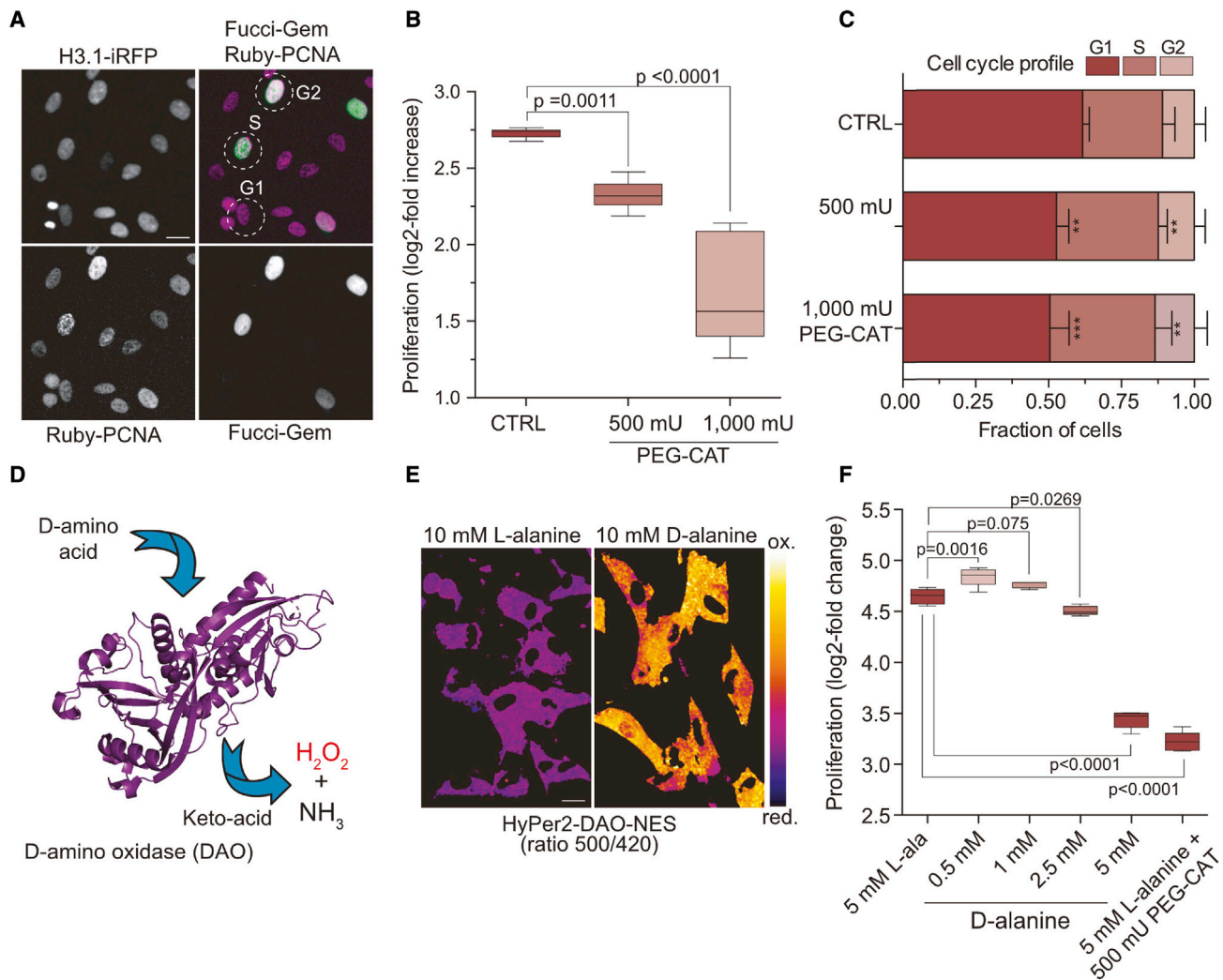


Figure 1. Proliferation and S phase progression require oxidative events in RPE-1 cells

(A) Single-cell analyses using cell cycle markers to classify cell cycle stages. Fucci-Gem-negative cells are in G1, Fucci-Gem-positive cells are in S or G2, and PCNA foci identify S phase as depicted in the overlay. Scale bars, 10 μ m.
 (B) Proliferation of RPE-1 cells in the presence of PEG-catalase (PEG-CAT). Boxplots indicate the median \log_2 -fold increase of cells for 48 h of PEG-CAT treatment. Significance according to one-way ANOVA with Dunnett's multiple comparisons test ($n = 3$, $N = 9$).
 (C) Stacked bars show the mean \pm SD cell cycle distribution of cells from (B), as classified in (A). Significance according to one-way ANOVA with Holm-Sidak's multiple comparisons test: ** (500 mU PEG-CAT(G1), $p = 0.0011$), *** (500 mU PEG-CAT(S), $p = 0.0032$), *** (1,000 mU PEG-CAT(G1), $p = 0.0001$), ** (1,000 mU PEG-CAT(S), $p = 0.0012$), ($n = 3$, $N = 9$).
 (D) D-amino acid oxidase (DAO)-mediated H_2O_2 production (PDB:1COI without ligands).
 (E) Ratio imaging of RPE-1 cells stably expressing cytoplasmic HyPer2-DAO-NES 1 h after the addition of 10 mM D- or L-alanine. Scale bars, 10 μ m.
 (F) Proliferation of RPE-1 cells in response to HyPer2-DAO-NES-produced H_2O_2 . Boxplots indicate the median \log_2 -fold change in proliferation after 48 h of treatment. Significance according to one-way ANOVA with Dunnett's multiple comparisons test ($N = 5$, data are representative of 3 independent experiments).

(~20%, Figure S1E). These measurements were performed at atmospheric oxygen concentration (21%), which might affect the redox status of cells that experience lower oxygen concentration in their *in vivo* tissue context. Thus, we repeated our measurements with RPE-1 cells grown at the oxygen concentration reported for the retinal epithelium (6.3%). These data were consistent and showed a steeper increase of ROS from G1 to S phase (Figure 2C). Measuring ROS in primary human foreskin fibroblasts (BJ) grown at their reported *in vivo* oxygen concentration (4%) gave a similar result (Figure 2D; Balin et al., 2002).

Notably, CellRox Deep Red labeling of RPE-1 cells appeared to be reminiscent of mitochondrial networks. Labeling of cells with CellRox Deep Red and the mitochondrial marker MitoTracker Green displayed overlapping signals (Figure 2E), suggesting that the cell cycle-correlated ROS dynamics we detected likely recapitulate changes in mitochondrial ROS. Indeed, detection of mitochondrial ROS with MitoSox Red dye mirrored the localization and cell cycle dynamics of overall ROS we observed (Figures 2E and 2F). An increase of mitochondrial ROS in S and G2/M could reflect mitochondrial activity, i.e.,

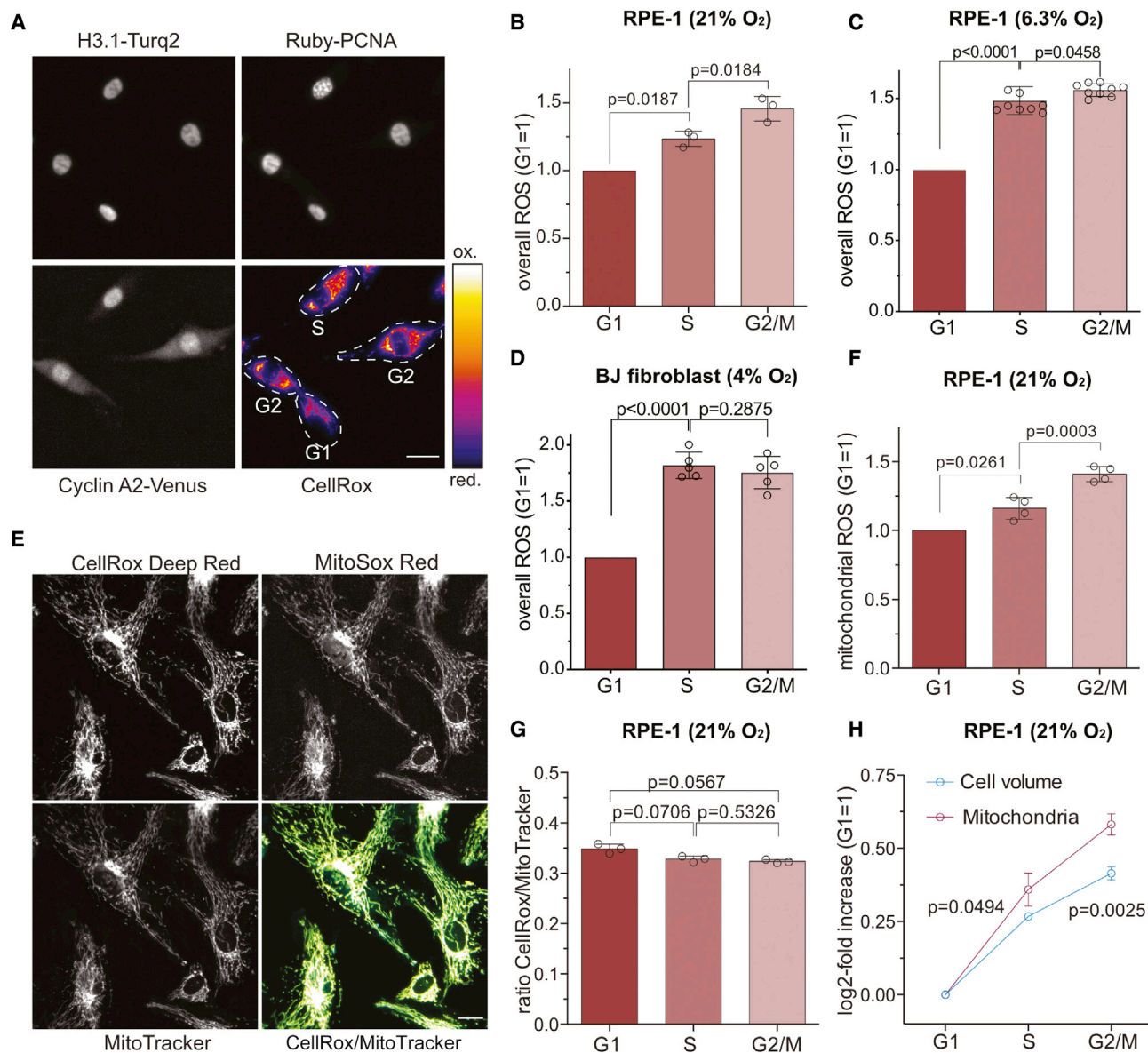


Figure 2. Mitochondrial ROS increase in S and G2 phase

(A) ROS detection in RPE-1 cells with CellRox Deep Red. Cell cycle classification based on cyclin A2-Venus and Ruby-PCNA (see also Figure S1B). Scale bars, 25 μ m.

(B and C) Flow cytometry analysis of RPE-1 cells stained with CellRox Deep Red grown at the indicated %O₂. Bars represent the mean \pm SD intensity normalized to G1 levels. Significance according to one-sample t test (G1 versus S) and two-tailed paired t test (S versus G2) (B, n = 3, N = 3; C, n = 3, N = 9).

(D) Equivalent analysis as in (C) with primary BJ fibroblasts grown at 4% O₂. Significance according to one-sample t test (G1 versus S) and two-tailed paired t test (S versus G2) (n = 4, N = 5).

(E) Co-labeling of RPE-1 cells with CellRox Deep Red, MitoSox Red, and MitoTracker Green. Overlay indicates CellRox (yellow) and MitoTracker (cyan) co-localization. Scale bars, 25 μ m.

(F) Flow cytometry analysis of RPE-1 cells stained with MitoSox Red. Bars represent the mean \pm SD intensity normalized to G1 levels. Significance according to one-sample t test (G1 versus S) and a two-tailed paired t test (S versus G2) (n = 4, N = 4).

(G) Flow cytometry analysis of RPE-1 cells co-labeled with CellRox Deep Red and MitoTracker. Bars represent the mean \pm SD CellRox/MitoTracker ratio. Significance according to paired one-way ANOVA with Holm-Sidak's multiple comparisons test (n = 3, N = 3).

(H) Flow cytometry quantification of cell volume and mitochondria based on forward scatter and MitoTracker Green. Data indicate the mean log₂-fold increase \pm SD normalized to G1 phase. Significance according to multiple t tests with Holm-Sidak's multiple comparisons test (n = 3, N = 3).

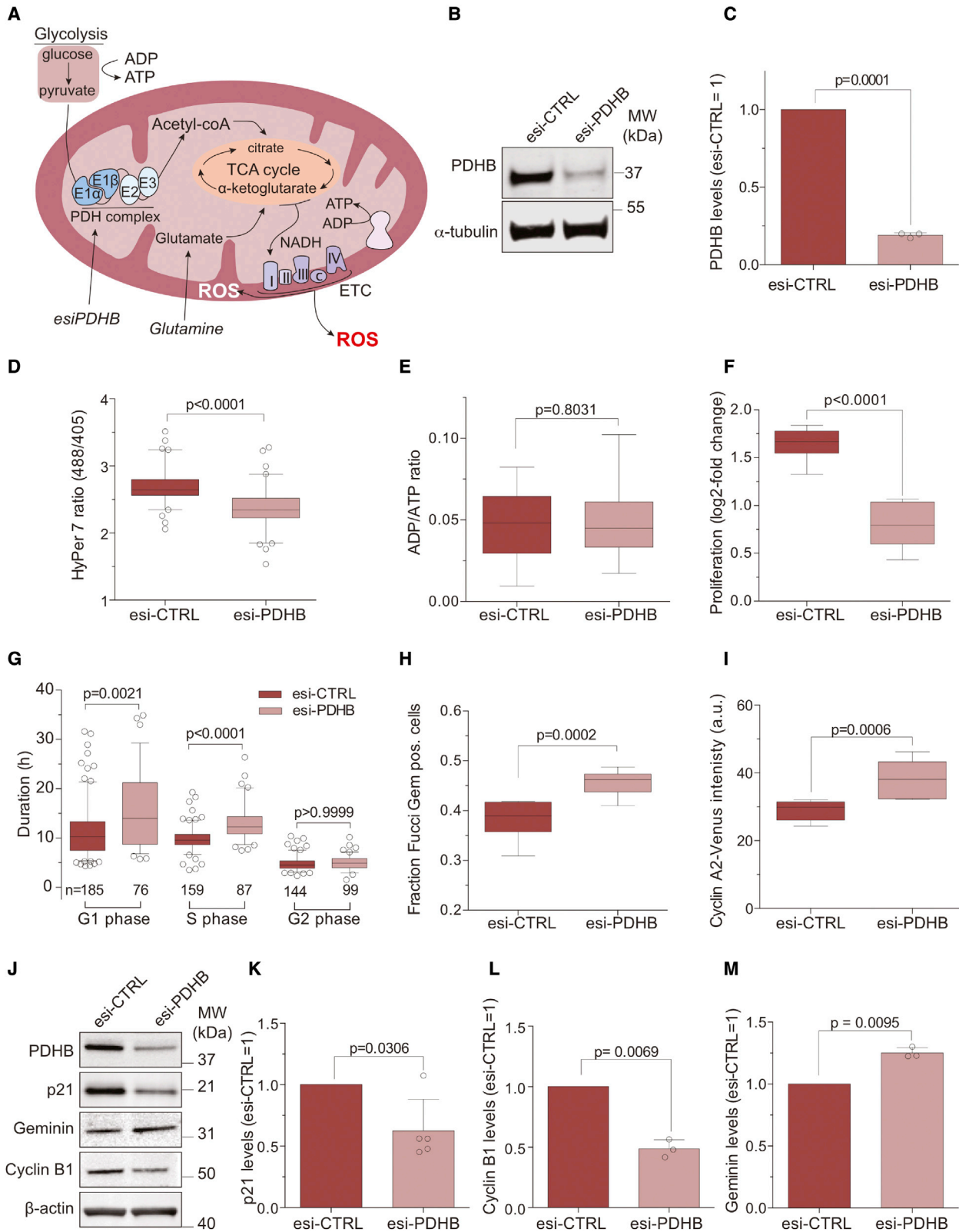


Figure 3. Mitochondrial ROS drive progression through S phase

(A) Illustration of mitochondrial metabolite, and ROS flux and the PDH complex as the gatekeeper between glycolysis and TCA cycle.

(B) Western blot analysis of cells treated for 48 h with control (esi-CTRL) or esiRNA targeting the β-subunit of the PDH complex (esi-PDHB).

(legend continued on next page)

due to metabolic switch from glycolysis to oxidative phosphorylation or increased mitochondria mass relative to cell volume. To test these possibilities, we performed flow cytometry analysis of cells stained for mitochondrial ROS with MitoSox Red and the overall mitochondrial content with membrane potential-independent dye MitoTracker Green. We observed an equal ratio of MitoSox Red to MitoTracker Green throughout the cell cycle, which implies that the increase of mitochondrial ROS is correlated to an increase in mitochondria (Figure 2G). Like others before (Havens et al., 2006), we observed that mitochondrial content increased faster than cell volume (Figure 2H), providing a possible explanation for the elevated concentrations of cellular ROS in S and G2 or M phases. Taken together, our data reveal that cellular ROS levels fluctuate during the cell cycle in both normoxic and physiological oxygen conditions, in a manner that correlates with mitochondrial ROS dynamics. Our data also suggest that the increase in cellular ROS largely results from a relative increase in mitochondria in S and G2/M compared with G1 phase.

Mitochondrial ROS drive progression through S phase

Mitochondrial ROS are produced as a by-product of oxidative phosphorylation. Thus, reducing the influx of metabolites into the tricarboxylic acid (TCA) cycle should decrease the amount of $O_2^{\cdot -}$ released from the electron transport chain (ETC) and limit the concentration of mitochondrial-derived H_2O_2 in the cytoplasm. We employed endoribonuclease-prepared siRNAs (esiRNAs) to downregulate PDHB, a subunit of the mitochondrial pyruvate dehydrogenase (PDH) complex that converts pyruvate to acetyl-CoA and acts as a gatekeeper between glycolysis in the cytosol and oxidative phosphorylation in mitochondria (Figure 3A). Depleting PDHB protein levels below 25% (Figures 3B and 3C) was sufficient to significantly reduce cellular H_2O_2 detected by HyPer7, a ratio-metric H_2O_2 sensor with improved sensitivity (Pak et al., 2020; Figure 3D). Importantly, reducing ROS production via PDHB depletion did not affect the ADP/ATP ratio indicating that cells were able to maintain ATP levels likely by glycolytic flux (Figure 3E).

PDHB-depleted cells proliferated slower (Figure 3F) but did not induce apoptosis based on PARP cleavage (Figure S1F). In support of our results from treatment with NAC and PEG-CAT (Figures 1 and S1) from single-cell time-lapse microscopy, PDHB-depleted cells took significantly longer to progress through S phase (Figure 3G). We noticed that PDHB depletion

in this experimental setup caused a more prolonged and heterogeneous duration of G1 phase. Unchanged ATP levels and decreased levels of p21, however, indicated that longer G1 phases were not caused by activation of a metabolic checkpoint that arrested cells at the G1/S transition (Jones et al., 2005; Mitra et al., 2009). Since we use PCNA foci to identify S phase and PDHB depletion reduced the number of PCNA foci (Figure 4), our analysis likely under-estimates the duration of S phase in favor of G1 phase (Zerjatke et al., 2017). We also assessed the cell cycle distribution of PDHB-depleted cells by western blotting for established cell cycle markers and by single-cell analyses for the S phase markers cyclin A2 and Fucci-Gem. Western blot analysis (Figure 3J) showed that the levels of G1 and G2 phase markers p21 and cyclin B1 were lower in PDHB-depleted cells (Figures 3K and 3L), whereas the S phase protein geminin accumulated (Figure 3M). In agreement with a delay in S phase but not G1 phase, PDHB depletion increased the proportion of Fucci-Gem-positive cells (Figure 3H) as well as cyclin A2-Venus intensity (Figure 3I), which are two markers that only accumulate after the G1/S transition. Our findings indicate that decreasing metabolic flux by interfering with the PDH complex reduces H_2O_2 to result in slower cell proliferation. The increased time required to progress through S phase and the accumulation of S, but not of G1 or G2 phase markers, supports a major cell cycle-associated role of mitochondrial ROS in S phase.

Mitochondrial ROS promote DNA replication

Since reducing mitochondrial ROS levels via PDHB depletion slowed S phase, we monitored the intensity and number of PCNA foci during time-lapse imaging as a surrogate to assess the fidelity of DNA replication. Replication foci in control cells showed the stereotypical spatiotemporal pattern described for replication factories (Leonhardt et al., 2000): multiple small foci in early S phase, concentration of foci in mid S phase, and formation of large clusters at the nuclear periphery in late S phase (Figure 4A; Video S1). In contrast, PCNA foci in PDHB-depleted cells were barely detectable until the very end of S phase at the same magnification used (Figure 4A; Video S2). To exclude potential off-target effects of esi-PDHB treatment, we targeted another subunit of the PDH complex, PDHA (Figure 4B). Quantifying the number of PCNA foci in S phase cells confirmed that depleting either PDHA or PDHB decreased the number of detectable PCNA foci in S phase (Figure 4C). To strengthen the link between mitochondrial ROS and DNA replication, we also

(C) Quantification of PDHB levels in (B) normalized to esi-CTRL. Bars indicate the mean \pm SD. Significance according to two-tailed one-sample t test ($n = 3$, $N = 3$).

(D) Analysis of H_2O_2 levels after PDHB depletion in RPE-1 cells stably expressing HyPer7. Boxplots indicate the median HyPer7 ratio. Significance according to two-tailed unpaired t test ($n = 3$, esi-CTRL $N = 80$, esi-PDHB $N = 82$).

(E) ATP quantification in response to PDHB depletion. Boxplots indicate the median ADP/ATP ratio. Significance according to two-tailed unpaired t test ($n = 3$, $N = 12$ esi-CTRL, $N = 11$, esi-PDHB).

(F) Proliferation of PDHB-depleted cells. Boxplots indicate the median \log_2 -fold change in proliferation. Significance according to two-tailed unpaired t test ($n = 3$, $N = 9$).

(G) Single-cell time-lapse analysis. Boxplots indicate the median duration of cell cycle phases. Significance according to Kruskal-Wallis' test and Dunnett's correction for multiple comparisons. ($n = 3$, N is indicated in the graph).

(H) Quantification of cells in S/G2 phase based on Fucci-Gem after treatment with esi-CTRL or esi-PDHB. Boxplots indicate the median fraction of Fucci-Gem-positive cells. Significance according to two-tailed unpaired t test ($n = 3$, $N = 9$).

(I) Quantification of cyclin A2-Venus expression after treatment with esi-CTRL or esi-PDHB. Boxplots indicate the median cyclin A2-Venus intensity. Significance according to two-tailed unpaired t test ($n = 3$, $N = 9$).

(J–M) (J) Western blot analysis of cell cycle markers after PDHB depletion, and (K–M) graphs showing quantification of the data normalized to esi-CTRL. Bars represent the mean \pm SD. Significance according to two-tailed one-sample t test ($n = 3$, $N = 5$ [p21], $N = 3$ [cyclin B1, geminin]).

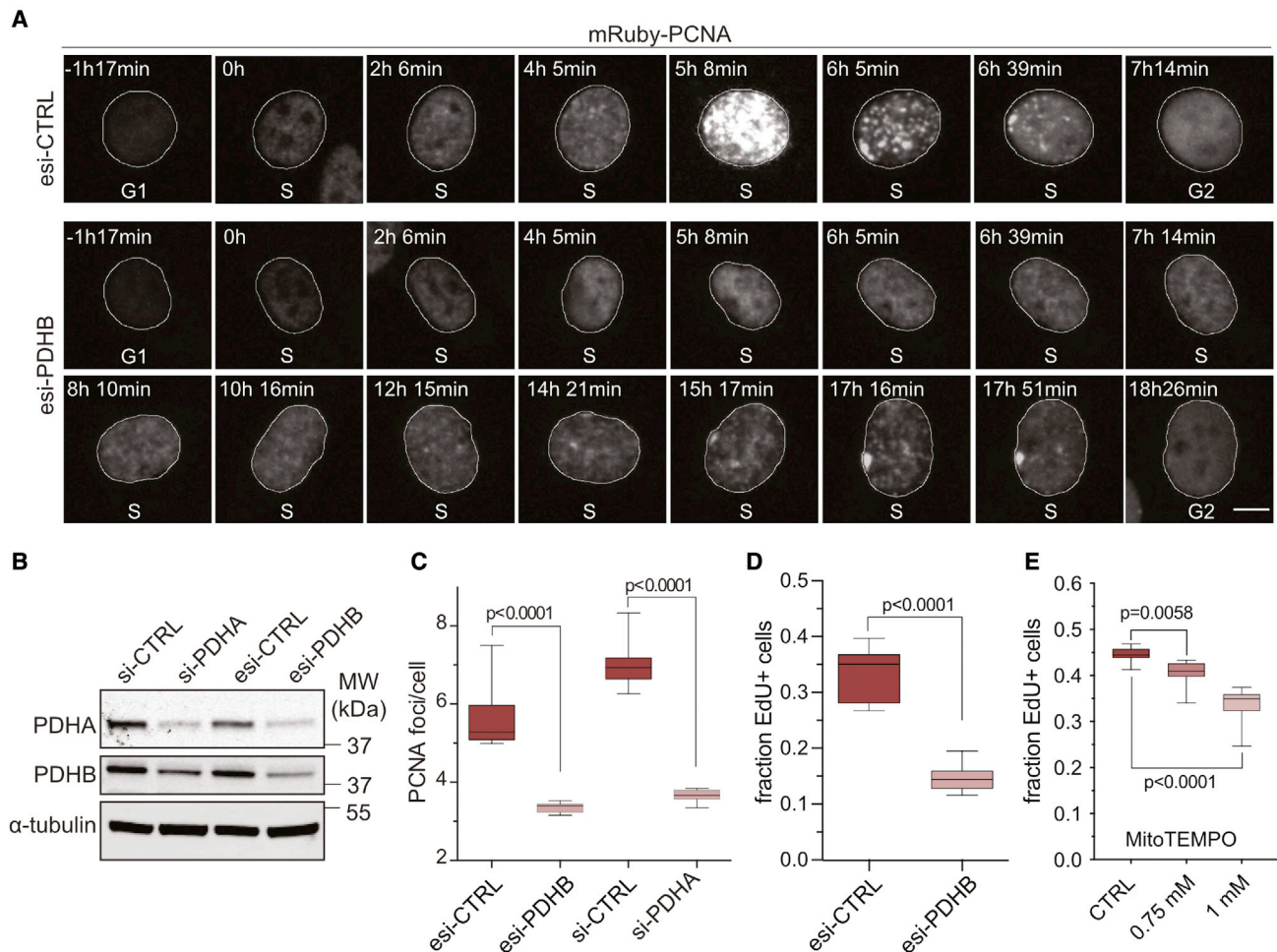


Figure 4. Mitochondrial ROS promote DNA replication

(A) Time-lapse images from the beginning ($t = 0$) to the end of S phase, highlighting PCNA foci formation in control (esi-CTRL) and PDHB-depleted cells (esi-PDHB) between 24 and 72 h after treatment. Scale bars, 20 μ m.

(B) Western blot analysis of esi orsi-RNA treated cells after 48 h. Note, targeting a PDH complex subunit results in partial co-depletion of the other.

(C) Quantification of PCNA foci in S phase in cells treated with esi/si-PDHB for 48 h. Boxplots indicate the median number of detectable foci. Significance according to two-tailed unpaired t test ($n = 3$, $N = 9$).

(D) Cells as treated in (A) were labeled with EdU and analyzed by single-cell imaging. Boxplots indicate the median fraction of EdU-positive cells. Significance according to two-tailed unpaired t test ($n = 3$, $N = 18$).

(E) EdU incorporation as in (D) but with RPE-1 cells treated for 48 h with MitoTEMPO. Boxplots indicate the median fraction of EdU-positive cells. Significance according to two-tailed unpaired t test ($n = 4$, $N = 15$: CTRL, 1 mM, $n = 2$, $N = 9$: 0.75 mM).

assessed 5-ethynyl-2'-deoxyuridine (EdU) incorporation in PDHB-depleted cells or cells treated for 48 h with the mitochondrial antioxidant MitoTEMPO. Indeed, both treatments significantly reduced the fraction of EdU-positive cells compared with the control (Figures 4D and 4E). Together, these data show that interfering with the TCA cycle and treatment with mitochondrial antioxidants affect DNA replication during S phase. Since interfering with the PDH complex reduced cellular H_2O_2 and hindered DNA replication, our findings support that mitochondrial ROS promote DNA replication.

CDK2 activity and T-loop phosphorylation are sensitive to mitochondrial ROS

CDK2 not only mediates the initiation of DNA replication but also regulates the spatiotemporal pattern of replication in

the nucleus (Sansam et al., 2015). Since we observed changes in PCNA foci formation and dynamics in response to PDH complex perturbation (Figure 4), we investigated whether mitochondrial ROS promote CDK2 activity in S phase. To assess CDK2 activity in living cells, we created an RPE-1 cell line with stable expression of a CDK2 activity sensor which is nuclear upon low CDK2 activity and becomes progressively more cytoplasmic as CDK2 activity increases (Spencer et al., 2013; Figure 5A). Depleting PDHB for 48 h strongly increased the number of cells with nuclear expression of the CDK2 sensor indicative of low CDK2 activity ($CDK2^{low}$) from 34% to 61% (Figures 5B and 5C). It is important to note that the $CDK2^{low}$ cells are unlikely to be quiescent or arrested before the restriction point (Spencer et al., 2013) because the same treatment resulted in the accumulation of multiple cell

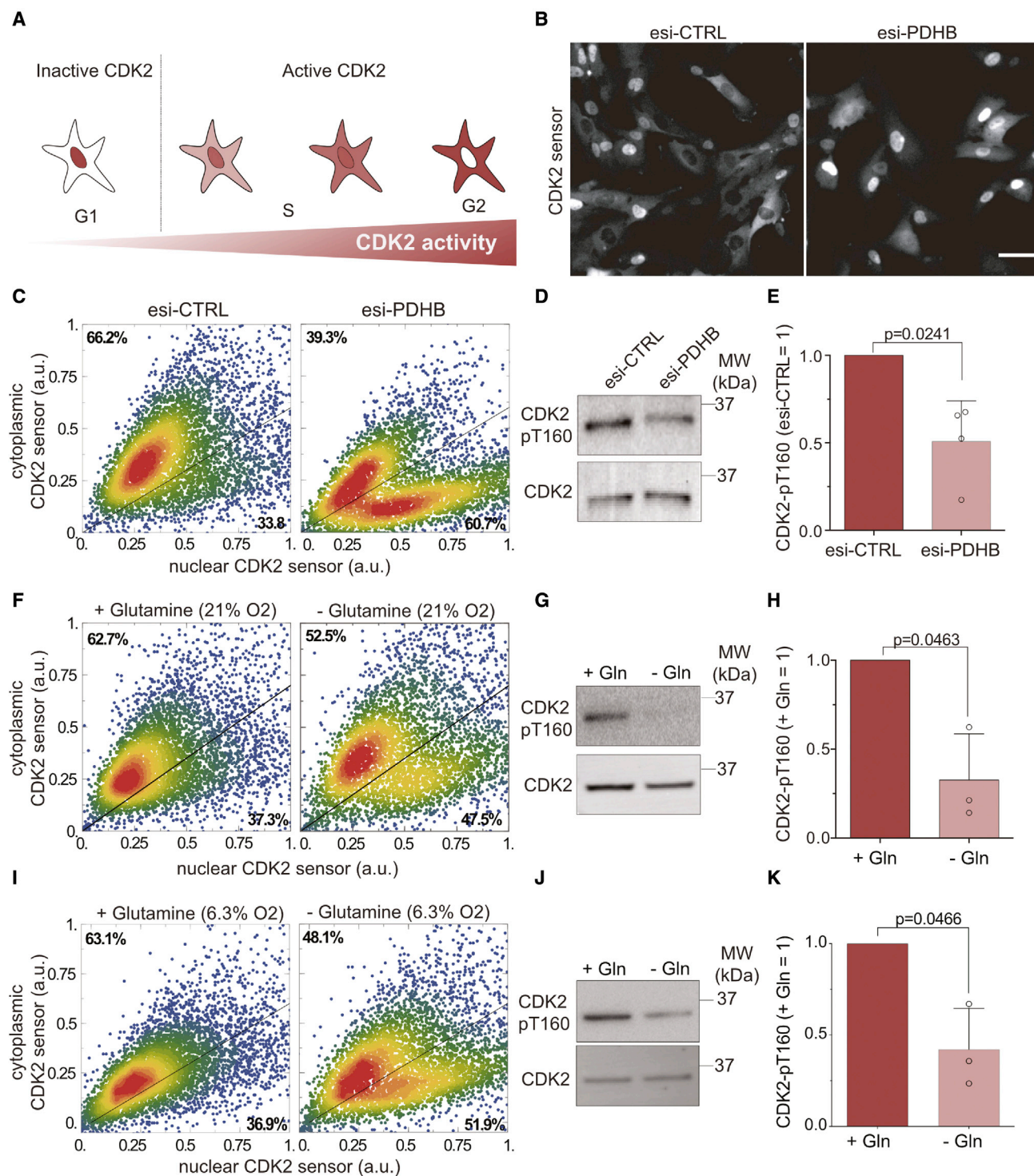


Figure 5. CDK2 activity and T-loop phosphorylation is sensitive to mitochondrial ROS

(A) Schematic showing CDK2-activity-dependent localization of the CDK2 sensor.

(B) CDK2 sensor localization in RPE-1 cells 48 h after esi-CTRL and esi-PDHB transfection. Note that the contrast of each image was adjusted separately to prevent the saturation of nuclear CDK2 sensor in esi-PDHB treatment. Scale bars, 50 μ m.

(C) Scatter plots show scaled intensities of cytoplasmic and nuclear CDK2 sensor in single cells, as treated in (B). The percentage of CDK2^{Low} and CDK2^{High} is indicated (n = 2, N = 6,000).

(D and E) (D) Western blot analysis of T160 phosphorylation from cells treated with esi-PDHB, and (E) quantification of the data. Bars indicate the mean \pm SD. Significance according to two-tailed one-sample t test (n = 4, N = 4).

(legend continued on next page)

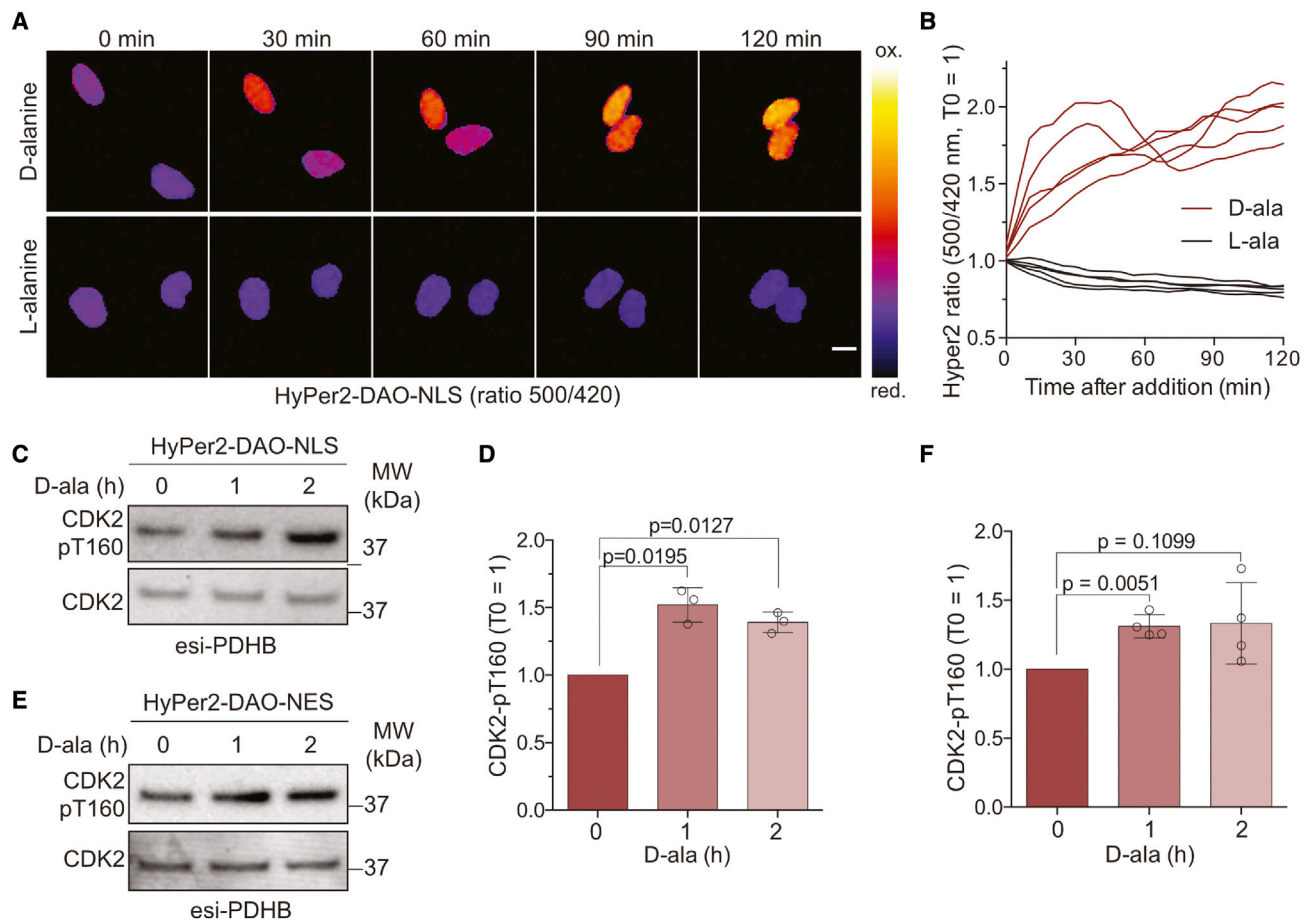


Figure 6. Genetically enabled ROS production increases T-loop phosphorylation

(A and B) (A) Ratio imaging of RPE-1 cells stably expressing nuclear HyPer2-DAO-NLS during 2 h of treatment with 10 mM D- or L-alanine (D-ala, L-ala), and (B) single-cell analysis of nuclear ROS production normalized to the ratio at $t = 0$. Scale bars, 10 μm .

(C and D) (C) Western blot analysis showing increased T160 phosphorylation in PDHB-depleted cells after D-ala-driven ROS production by HyPer2-DAO-NLS, and (D) quantification of T160 phosphorylation levels. Bars represent the mean \pm SD normalized to $t = 0$. Significance according to two-tailed one-sample t test ($n = 3$, $N = 3$).

(E and F) (E) Western blot analysis with cytoplasmic ROS production by HyPer2-DAO-NES, and (F) quantification data. Bars represent the mean \pm SD normalized to $t = 0$. Significance according to two-tailed one-sample t test ($n = 4$, $N = 4$).

cycle markers expressed downstream of the G1/S transition, such as cyclin A2 and geminin (Figure 3).

Next, we addressed how mitochondrial metabolism and ROS production affect CDK2 activity on the molecular level. Full activity of CDK2 requires binding of E or A-type cyclins and phosphorylation of T160 within its T-loop. Because PDHB-depleted cells can enter S phase as indicated by an increase of Fucci-Gem-positive cells (Figure 3H) and express cyclin A2 (Figure 3I), we investigated whether T160 phosphorylation was impacted. Indeed, quantitative western blot analysis of lysates from control

and PDHB-depleted cells with a phosphorylation-specific T160 antibody (CDK2 pT160) showed a $\sim 50\%$ reduction in T-loop phosphorylation (Figures 5D and 5E). Importantly, this difference was not due to an enrichment of PDHB-depleted cells in G1 phase since repeating the experiment in cells synchronized at the beginning of S phase with thymidine gave a comparable result (Figures S2A and S2B). To confirm these findings, we also starved cells of glutamine (Gln) for 6 h to reduce mitochondrial ROS production (Oh et al., 2020). As with depleting PDHB, 6 h of Gln starvation strongly increased the number of CDK2^{low}

(F) Scatter plots show scaled intensities of cytoplasmic and nuclear CDK2 sensor in single cells after 6 h of glutamine (Gln) starvation at 21% O₂ ($n = 3$, $N = 6,000$). (G and H) (G) Western blot analysis detecting T160 phosphorylation in cells treated with glutamine starvation (–Gln) and (H) quantification of the data. Bars indicate the mean \pm SD. Significance according to two-tailed one-sample t test ($n = 3$, $N = 3$).

(I) Equivalent analysis as (F) but with RPE-1 cells grown at 6.3% O₂ ($n = 3$, $N = 6,000$).

(J) Western blot analysis and (K) quantification of T160 phosphorylation from cells grown at 6.3% O₂ as in (G) and (H). Bars indicate the mean \pm SD. Significance according to two-tailed one-sample t test ($n = 3$, $N = 3$).

cells in both normoxic (21% O₂) and physiological (6.3% O₂) oxygen conditions (Figures 5F and 5I) and reduced T160 phosphorylation (Figures 5G, 5H, 5J, and 5K). Importantly, 6 h of Gln starvation did not synchronize cells in G1 phase, where pT160 is intrinsically lower (Figure S2C). Finally, addition of 8 and 10 mM NAC for 5 h to S phase cells also reduced T160 phosphorylation, although to a lesser extent (Figures S2D and S2E). Exposure of cells to different concentrations of NAC for 48 h, similar to proliferation experiments in Figure S1, decreased pT160 by up to 83% (Figure S2G) and resulted in accumulation of the CDK2 sensor in nuclei indicative of reduced CDK2 activity (Figure S2F). Importantly, the fraction of cyclin A2-positive cells increased upon NAC treatment in agreement with a delay in S phase but not in G1 (Figure S2H). Collectively, our data show that reducing conditions achieved by metabolic perturbation of oxidative phosphorylation or a chemical reductant decreased T-loop phosphorylation of CDK2, and thus, the degree of CDK2 activity is coupled to mitochondrial metabolism by ROS.

Genetically enabled ROS production increases T-loop phosphorylation

Thus far, our experiments in reducing conditions demonstrate indirectly that ROS are involved in regulating CDK2 activity via T160 phosphorylation. For more direct evidence, we tested if the loss of T160 phosphorylation after PDHB depletion can be rescued by DAO-mediated H₂O₂ production (Figure 1). As CDK2-cyclin E/A complexes are predominantly nuclear, we created an RPE-1 cell line that stably expresses DAO fused to a nuclear localization sequence (NLS, HyPer2-DAO-NLS) that can rapidly generate ROS in response to D- but not to L-alanine (Figures 6A and 6B). Based on the gradual increase in the HyPer2 ratio (Figure 6B), we induced H₂O₂ for 1 and 2 h and evaluated the consequences on T160 phosphorylation in PDHB-depleted cells. 1 h of stimulating H₂O₂ production from nuclear DAO was sufficient to increase T160 phosphorylation significantly (Figures 6C and 6D). Because H₂O₂ produced from mitochondria needs first to pass the nuclear membrane to reach CDK2-cyclin E/A complexes, we repeated the experiment with cytoplasmic HyPer2-DAO-NES (Figure 1E). Cytoplasmic H₂O₂ production also rescued T160 phosphorylation (Figures 6E and 6F), indicating

that mitochondrial ROS can target CDK2 which is predominantly nuclear. These data show that genetically enabled H₂O₂ production promotes T-loop phosphorylation on CDK2. The observation that cytoplasmic production of H₂O₂ can target nucleoplasmic CDK2 further supports that mitochondrial ROS can regulate CDK2 activity by acting as a signaling molecule.

Preventing C177 oxidation increases KAP binding to CDK2

Our finding that ROS stimulate CDK2 T-loop phosphorylation led us to hypothesize that either CDK2 itself or the enzymes that regulate T160 phosphorylation (CAK and KAP) are targeted by ROS. To evaluate these possibilities, we took advantage of the membrane-permeant, chemoselective probe BTM to label sulfenic acids in living cells (Gupta and Carroll, 2016). After labeling RPE-1 cells with BTM for 30 min, we performed click chemistry and a streptavidin pull-down to purify sulfenic acid-modified proteins (Figures 7A and S3A). In support of CDK2 oxidation, we detected CDK2 and known sulfenic acid-modified protein glyceraldehyde 3-phosphate dehydrogenase (GAPDH) in our pull-downs, but not highly abundant ribosomal protein RPL26 which does not contain any cysteine residues (Figure 7B). This is in agreement with several mass spectrometry studies using BTM or alternative probes in H₂O₂-treated cell extracts or unperturbed cells identifying CDK2 oxidation to sulfenic acid on C177 (Yang et al., 2015; Gupta et al., 2017; Xiao et al., 2020; Shi et al., 2021). C177 is positioned in an unstructured loop near T160 (Figure S3B), conserved in vertebrates (Figure S3C) and only found in CDK2 and not in other related human CDKs (Figure 7C). Next, we assessed whether CDK2 oxidation increases from G1 to S and G2 phase as predicted with an increase in ROS levels during the cell cycle. We expressed CDK2 with a C-terminal hemagglutinin (HA) tag in RPE-1 cells and released them from serum starvation for 8, 18, and 22 h to be synchronized to G1, S, and G2, respectively (Figures S3D and S3E). After labeling with BTM for 30 min, we lysed the cells under reducing conditions and conjugated the fluorescent dye Az800 to BTM by click chemistry (Figure S3F). Detection of Az800 on CDK2-HA immunoprecipitates revealed that cysteine oxidation on CDK2 to sulfenic acid increased from G1 phase to S and G2 phase in a manner

(C) Clustal Omega alignment of T-loop and C177 of human CDKs.

(D) SDS-PAGE gel scan and quantification of BTM-labeled CDK2-HA purified from cells synchronized to G1, S, and G2 phases. Significance according to two-tailed one-sample t test. Full scans at lower intensities are shown in Figure S3F (n = 3, N = 3).

(E–G) (E) Western blot analysis of StreptII pull-downs from S-phase-synchronized RPE-1 cells expressing CDK2-WT-StreptII (WT), CDK2-C177S-StreptII (C177S), or CDK6-StreptII as a control, and quantification of pT160 (F) and cyclin A2 binding (G). Bars represent the mean ± SD. Significance according to two-tailed one-sample t test (pT160: n = 6, N = 6; cyclin A2: n = 4, N = 4).

(H and I) (H) Interaction between recombinant GST-KAP and CDK2-StreptII purified from S phase cells and (I) quantification of the data. Silver staining of a StreptII pull-down is shown in Figure S3H. Bars represent the mean ± SD. Significance according to two-tailed unpaired one-sample t test (KAP: n = 4, N = 4).

(J and K) Western blots showing the binding of (J) endogenous KAP to CDK2-StreptII from S phase cells with or without DTT (n = 3), and (K) WT and C177S CDK2-HA from lysates prepared without DTT (n = 3). Arrow indicates KAP signal.

(L) Proliferation of RPE-1 CDK2^{as} cells expressing ectopic CDK2 WT or C177S in the presence of 3MB-PP1 or 6-BAP control (n = 3). 3MB-PP1 inactivates endogenous CDK2^{as} but not ectopic CDK2. Significance according to two-way ANOVA with Dunnett's multiple comparisons test; p values comparing 3MB-PP1-treated WT and C177S cells are shown (N = 12).

(M) Competitive growth analysis of CDK2 WT and C177S cells in the presence of 3MB-PP1. Boxplots indicate the median ratio of WT/C177S cells normalized to the mean on day 0. Significance according to Kruskal-Wallis' test with Dunnett's correction for multiple comparisons (n = 3, N = 18).

(N) EdU incorporation of CDK2 WT and C177S cells in the presence of 3MB-PP1 after G1 phase synchronization by palbociclib (n = 3). Boxplots indicate the median fraction of EdU-positive cells. Significance according to one-way ANOVA with Sidak's correction for multiple comparisons (N = 6).

(O) Model of ROS-regulated CDK2-KAP interaction during G1 and S phase, where C177 is reduced (blue) during G1 phase to allow KAP recruitment and dephosphorylation of T160. Oxidation of C177 (red) by increasing mitochondrial ROS in S phase prevents KAP binding and shifts the balance toward CAK binding. Thus, high CDK2 activity can be maintained in the presence of KAP.

that reflected the increase of ROS during the cell cycle we observed (compare [Figure 2](#) and [Figure 7D](#)). To investigate the relationship between C177 oxidation and T160 phosphorylation, we mutated C177 to cysteine-mimetic serine (C177S) or alanine (C177A) and expressed these mutant constructs tagged with StrepII into RPE-1 cells synchronized to the beginning of S phase. StrepII pull-downs showed that T160 phosphorylation on the C177S ([Figures 7E and 7F](#)) and C177A ([Figures S3G and S3H](#)) mutants were markedly reduced, whereas binding of cyclin A2 ([Figures 7G and S3I](#)) and cyclin E1 ([Figures S3J and S3K](#)) was not significantly impacted.

One possibility is that C177 oxidation regulates the binding of CAK or KAP to CDK2 and, therefore, impacts the phosphorylation status of T160. To test this, we compared the binding of recombinant CAK and KAP with CDK2-StrepII WT and C177S purified from cells synchronized to S phase when CDK2 should be oxidized ([Figure S4A](#)). For CAK binding assays, we first dephosphorylated CDK2-StrepII WT and C177S immobilized on beads with λ -phosphatase ([Figure S4B](#)) before adding recombinant CAK in the presence or absence of the reducing agent dithiothreitol (DTT) ([Figure S4C](#)). Here, we did not observe significant changes in CAK binding to CDK2 by western blotting for CDK7 ([Figure S4D](#)). In contrast, when we assessed the binding of recombinant KAP to phosphorylated CDK2, we found that KAP binding was increased 2-fold for the C177S mutant compared with the WT in the absence of DTT ([Figures 7H and 7I](#)). In the presence of DTT, KAP binding selectively increased for CDK2 WT but not for the C177S mutant ([Figure 7I](#)). Finally, we tested whether endogenous KAP binds to CDK2 in a redox-dependent manner. We performed CDK2 pull-downs from lysates of S phase-synchronized cells treated with or without DTT for 10 min. Indeed, endogenous KAP was only detected in CDK2 pull-downs under reducing conditions and not without DTT in the extract preparation ([Figure 7J](#)). In contrast, HA-tagged CDK2 C177S but not WT was able to pull-down endogenous KAP in the absence of DTT, suggesting that mutation of C177S is sufficient to render the CDK2-KAP interaction insensitive to oxidation ([Figure 7K](#)).

If CDK2 oxidation on C177 is important for full CDK2 activation and S phase progression then cells expressing C177S in the absence of endogenous CDK2 activity should be impaired in proliferation and DNA replication. Since C177 is vital to proliferation, we were hesitant to introduce a C177S mutation directly to the endogenous CDK2 gene. Instead, we created pools of 5 independent stable cell lines expressing untagged CDK2 WT or C177S in RPE-1 cells harboring two alleles of Shokat analog sensitive CDK2 (CDK2^{as}) ([Merrick et al., 2011](#)). This allowed us to rapidly inactivate endogenous CDK2 and assess how mutant C177S CDK2 can promote proliferation and DNA replication compared with WT CDK2. Indeed, addition of inhibitory Shokat ATP analog 3MB-PP1 but not of non-inhibitory 6-benzylaminopurine (6-BAP) decreased the proliferation of parent CDK2^{as} cells ([Figure 7L](#)), as previously reported ([Merrick et al., 2011](#)). Cells expressing CDK2 WT were only mildly affected by 3MB-PP1 since ectopic CDK2 is not analog sensitive. In contrast, expression of C177S slowed proliferation similar to 3MB-PP1-treated parent CDK2^{as} cells, regardless of whether 3MB-PP1 was added. This suggests that the C177S mutant has dominant-negative properties, consistent with known CDK

T-loop mutants ([van den Heuvel and Harlow, 1993](#)). Moreover, CDK2 WT cells proliferated faster than C177S expressing cells ([Figure 7M](#)), which was not due to less expression of ectopic CDK2 since C177S was expressed more than WT ([Figures S4F and S4G](#)). Finally, we assessed the ability of C177S to promote DNA replication. To account for potential differences in cell cycle distribution between WT and C177S cells, we synchronized the cells to G1 phase by treating them with CDK4/6 inhibitor palbociclib for 24 h ([Trotter and Hagan, 2020](#)). We released cells in the presence of EdU and evaluated EdU incorporation 4 and 6 h later for early and mid S phase, respectively ([Figure S4E](#); [Trotter and Hagan, 2020](#)). In agreement with our conclusion that C177 oxidation promotes CDK2 activity and DNA replication, there were fewer EdU-positive cells for the C177S mutant compared with WT ([Figure 7N](#)). Collectively, these data demonstrate that oxidation of C177 located near the T-loop is important to maintain complete T160 phosphorylation and optimal CDK2 activity. Mutation of C177 or reducing CDK2 oxidation increased KAP binding, which supports that ROS promote S phase progression and DNA replication by preventing T160 phosphatase recruitment.

DISCUSSION

To proliferate, cells must coordinate cell growth driven by metabolism and cell cycle progression to ensure that DNA and other essential cellular components are duplicated before cell division. Bidirectional cross-talk between cell cycle and metabolic regulation are emerging topics of active research, especially because aberrations in either system are hallmarks of numerous diseases including cancer. In the present study, we uncover that mitochondrial ROS levels continuously increase from G1 to S and G2 phases and oxidize CDK2. Oxidation occurs at a conserved cysteine residue close to the T-loop of CDK2 and prevents the binding of KAP. As a consequence, T-loop phosphorylation can be sustained despite high KAP expression during early S phase (Gyuris et al., 1993), guaranteeing complete CDK2 activation and S phase progression. Thus, we identify a simple and elegant mechanism by which cell cycle-dependent production of mitochondrial ROS promote DNA replication to coordinate cell cycle progression with the metabolic state of the cell.

The concept that the redox environment of cells is coordinated with cell cycle progression dates back to 1931 when Rapkine ([Rapkine, 1931](#)) postulated a thiol cycle in dividing urchin eggs. Since then, redox fluctuations similar to the ROS dynamics we report have been inferred by several studies indirectly by reducing agents such as NAC ([Menon et al., 2007](#); [Kim et al., 2001](#); [Kyaw et al., 2004](#); [Havens et al., 2006](#)) or directly by the ROS-sensitive fluorescent probe dichlorodihydrofluorescein diacetate DCFH-DA ([Kim et al., 2001](#); [Kyaw et al., 2004](#); [Havens et al., 2006](#); [Menon and Goswami, 2007](#); [Ivanova et al., 2021](#)). ROS measurements with DCFH-DA are inherently prone to artifacts and have several limitations ([Kalyanaraman et al., 2012](#); [Bonini et al., 2006](#)). Therefore, the source and dynamics of ROS levels during the cell cycle in proliferating cells have remained controversial. In our study, we used non-transformed RPE-1 cells and the ROS probe CellRox Deep Red, which labels the hydroxyl radical, O₂^{•-} and H₂O₂ in order of sensitivity. We find that CellRox Deep Red predominately labels mitochondrial

structures in living cells, which is consistent with O₂⁻ production in mitochondria. Our data suggest that the cell cycle-dependent increase of cellular ROS likely recapitulates the relative increase in mitochondrial content rather than increased respiration (Figure 2). We cannot, however, exclude that bursts of mitochondrial activity undetectable by our analyses could also contribute to ROS production, such as during the G1/S transition (Mitra et al., 2009).

Previous studies have suggested that mitochondria in *Drosophila* and human cells are needed to provide the energy and buildup of cyclin E required to enter S phase (Mandal et al., 2005; Mitra et al., 2009; Robbins and Morrill, 1969). Our work identifies that mitochondrial ROS are a key driver of S phase by ensuring full CDK2 activity necessary for DNA replication (Figures 1, 3, and 4). We find no evidence that restricting the metabolic influx of acetyl-CoA into the TCA cycle decreases ATP levels and activates a metabolic checkpoint that restricts entry into S phase in a p53- and p21-dependent manner (Figure 3; Jones et al., 2005; Mitra et al., 2009). Furthermore, mitochondrial ATP production appears to be dispensable for human cells with access to sufficient glucose (Sullivan et al., 2015). Towards the end of G1 phase, mitochondria form a transient hyperfused network that drives cells into S phase, by an undefined mechanism that possibly involves p53 and boosting the levels of cyclin E (Mitra et al., 2009). Our data indicate that a limiting function of ROS is downstream of this process because cells with decreased levels of mitochondrial ROS display elevated levels of the S and G2 phase markers geminin and cyclin A2 (Figure 3). Thus, mitochondria seem to employ two sequential and distinct mechanisms to regulate S phase via CDK2 activity: energy-driven expression of cyclin E to initiate S phase and ROS-sustained T-loop phosphorylation to drive DNA replication.

30 years after the discovery of T-loop phosphorylation (Gould et al., 1991), a congruent model explaining how CAK and KAP activities are coordinated to avoid unnecessary cycles of phosphorylation and de-phosphorylation is lacking. In higher organisms, CDK2 and CDK1 are the only regulatory CDKs that sequentially bind to different cyclins during the cell cycle and thus can become a target of KAP as monomers, i.e. during the degradation of cyclin E in early S phase and of cyclin A during prometaphase. However, in contrast to CDK2, CAK and KAP never compete for CDK1 because CDK1 is only phosphorylated by CAK once the cyclin is bound, and in this state, the T-loop is inaccessible to KAP (Poon and Hunter, 1995; Song et al., 2001). For CDK2, however, the T-loop becomes accessible to KAP once CDK2 switches from cyclin E to cyclin A at the beginning of S phase, and yet T160 phosphorylation remains constant until the end of mitosis (Figure S3D). Our finding that the interaction between CDK2 and KAP is regulated by oxidation of C177 (Figure 7) addresses this critical issue and explains why T160 phosphorylation is sensitive to mitochondrial ROS production (Figure 5). Regulation of CDK2 activity by this unique oxidative mechanism could potentially be exploited to develop CDK2-specific inhibitors that do not target closely related kinases, i.e., by a cysteine-reactive probe that prevents C177 oxidation but still allows for KAP binding.

We propose a model by which the increase in mitochondrial ROS in S phase prevents KAP binding to CDK2 to ensure that T-loop phosphorylation of CDK2 can be sustained at times of

high KAP expression (Gyuris et al., 1993; Figure 7O). An exception to this rule would include CDK2 in *Drosophila* which has no C177, but here, CDK2 does not switch between cyclins because cyclin A only interacts with CDK1 in this organism (Harper and Elledge, 1998). A cysteine in the position of C177 is also absent in unicellular organisms and plants, where the function of CDK2 is carried out by CDK1.

The structure of KAP in association with CDK2 pT160 presents no clear evidence of how C177 oxidation could hinder KAP binding (Song et al., 2001). However, only residues 25–198 of KAP are resolved and truncation of residues 1–34 completely abolishes its interaction with CDK2 (Yeh et al., 2003). Hence, it is conceivable that the N terminus of KAP directly binds to CDK2 in a C177 oxidation-sensitive manner. Alternatively, we are currently investigating whether another interactor binds to CDK2 in more oxidizing conditions and thereby prevents the recruitment of KAP.

Limitations of the study

Although proteomics identified C177 as the only oxidized cysteine of CDK2 (Yang et al., 2015; Gupta et al., 2017; Xiao et al., 2020; Shi et al., 2021), we cannot exclude that the other two cysteines of CDK2 can be oxidized as well. The crystal structure of CDK2, however, indicates that only C177 is solvent exposed (Brown et al., 1999). KAP itself contains several redox-sensitive cysteines (Xiao et al., 2020), and cysteine 140 which is crucial for KAP activity is readily oxidized *in vitro* (Song et al., 2001). Thus, the increase of ROS during S and G2 phase might also negatively regulate KAP activity or its interaction with CDK2 to feedback to CDK2 activity. Our data imply that the levels of ROS and CDK2 oxidation are reduced once cells enter the next cycle. Whether this is a consequence of diminished ETC activity in mitosis/early G1 phase or an active process that might involve the antioxidant system or CDK2 turnover are intriguing questions to be addressed in the future.

STAR★METHODS

Detailed methods are provided in the online version of this paper and include the following:

- KEY RESOURCES TABLE
- RESOURCE AVAILABILITY
 - Lead contact
 - Materials availability
 - Data and code availability
- EXPERIMENTAL MODEL AND SUBJECT DETAILS
 - Cell lines and cell culture
 - Plasmids and cell line generation
- METHOD DETAILS
 - Cell treatments
 - RNA interference
 - Proliferation experiments and EdU detection
 - Lysate, extracts and interaction studies
 - BTM labeling
 - SDS-PAGE and Western blot analyses
 - ROS labeling
 - ADP/ATP ratio
 - Microscopy
- QUANTIFICATION AND STATISTICAL ANALYSIS

- Image analysis
- Statistical methods

SUPPLEMENTAL INFORMATION

Supplemental information can be found online at <https://doi.org/10.1016/j.devcel.2022.06.008>.

ACKNOWLEDGMENTS

We thank K. Carroll and A. Nadler for providing BTD, V. Belousov for HyPer7 and HyPer2-DAO constructs, S. Spencer for CDK2 sensor, R. Fisher for RPE-1 CDK2^{as} cells and experimental suggestions, T.D. Vu and M. Cuenca for help with single-cell tracking and ratio analysis, A. Radzishchanskaya for advice on cell competition, J. Pines for critical reading of the manuscript, and members of the Mansfeld laboratory for technical help and discussions. J.M. receives funding from the European Research Council under the European Union's Horizon 2020 research and innovation program (ERC starters grant: 680042) and is supported by the Institute of Cancer Research (ICR) London. D.G.K., K.J., and J.V. are members of the Dresden Biomedicine and Bioengineering PhD program. J.K.L. receives funding from the ICR/RM CRUK RadNet Centre of Excellence (grant: A28724). We acknowledge support from the Light Microscopy and Flow Cytometry Facilities of the Center for Molecular and Cellular Bioengineering (TU Dresden) and the Chelsea Light Microscopy Facility (ICR).

AUTHOR CONTRIBUTIONS

Conceptualization, J.M. and D.G.K.; methodology, D.G.K., K.J., J.V., T.Z., I.G., and J.M.; investigation, D.G.K., K.J., J.V., J.K.L., and J.M.; writing—original draft, D.G.K., K.J., and J.M.; writing—revised manuscript, K.J., J.K.L., and J.M.; funding acquisition, I.G. and J.M.; supervision, I.G. and J.M.

DECLARATION OF INTERESTS

The authors declare no competing interests.

Received: March 8, 2021

Revised: April 13, 2022

Accepted: June 14, 2022

Published: July 7, 2022

REFERENCES

Adusumilli, V.S., Walker, T.L., Overall, R.W., Klatt, G.M., Zeidan, S.A., Zocher, S., Kirova, D.G., Ntitsias, K., Fischer, T.J., Sykes, A.M., et al. (2021). ROS Dynamics Delineate functional states of hippocampal neural stem cells and link to their activity-dependent exit from quiescence. *Cell Stem Cell* **28**, 300–314.e6.

Ahmed Alfar, E., Kirova, D., Konantz, J., Birke, S., Mansfeld, J., and Ninov, N. (2017). Distinct levels of reactive oxygen species coordinate metabolic activity with beta-cell mass plasticity. *Sci. Rep.* **7**, 3994.

Armstrong, L., Tilgner, K., Saretzki, G., Atkinson, S.P., Stojkovic, M., Moreno, R., Przyborski, S., and Lako, M. (2010). Human induced pluripotent stem cell lines show stress defense mechanisms and mitochondrial regulation similar to those of human embryonic stem cells. *Stem Cells Dayt. Ohio* **28**, 661–673.

Balin, A.K., Pratt, L., and Allen, R.G. (2002). Effects of ambient oxygen concentration on the growth and antioxidant defenses of human cell cultures established from fetal and postnatal skin. *Free Radic. Biol. Med.* **32**, 257–267.

Bedard, K., and Krause, K.H. (2007). The NOX family of ROS-generating NADPH oxidases: physiology and pathophysiology. *Physiol. Rev.* **87**, 245–313.

Bodnar, A.G., Ouellette, M., Frolkis, M., Holt, S.E., Chiu, C.P., Morin, G.B., Harley, C.B., Shay, J.W., Lichtsteiner, S., and Wright, W.E. (1998). Extension of life-span by introduction of telomerase into normal human cells. *Science* **279**, 349–352.

Bonini, M.G., Rota, C., Tomasi, A., and Mason, R.P. (2006). The oxidation of 2',7'-dichlorofluorescein to reactive oxygen species: a self-fulfilling prophesy? *Free Radic. Biol. Med.* **40**, 968–975.

Brown, N.R., Noble, M.E., Lawrie, A.M., Morris, M.C., Tunnah, P., Divita, G., Johnson, L.N., and Endicott, J.A. (1999). Effects of phosphorylation of threonine 160 on cyclin-dependent kinase 2 structure and activity. *J. Biol. Chem.* **274**, 8746–8756.

Burhans, W.C., and Heintz, N.H. (2009). The cell cycle is a redox cycle: linking phase-specific targets to cell fate. *Free Radic. Biol. Med.* **47**, 1282–1293.

Cheng, A., Ross, K.E., Kaldis, P., and Solomon, M.J. (1999). Dephosphorylation of cyclin-dependent kinases by type 2C protein phosphatases. *Genes Dev.* **13**, 2946–2957.

Chiu, J., and Dawes, I.W. (2012). Redox control of cell proliferation. *Trends Cell Biol.* **22**, 592–601.

Collin, P., Nashchekina, O., Walker, R., and Pines, J. (2013). The spindle assembly checkpoint works like a rheostat rather than a toggle switch. *Nat. Cell Biol.* **15**, 1378–1385.

Connor, K.M., Subbaram, S., Regan, K.J., Nelson, K.K., Mazurkiewicz, J.E., Bartholomew, P.J., Aplin, A.E., Tai, Y.T., Aguirre-Ghisso, J., Flores, S.C., et al. (2005). Mitochondrial H₂O₂ regulates the angiogenic phenotype via PTEN oxidation. *J. Biol. Chem.* **280**, 16916–16924.

Desai, D., Wessling, H.C., Fisher, R.P., and Morgan, D.O. (1995). Effects of phosphorylation by CAK on cyclin binding by CDC2 and CDK2. *Mol. Cell Biol.* **15**, 345–350.

Fesquet, D., Labbé, J.C., Derancourt, J., Capony, J.P., Galas, S., Girard, F., Lorca, T., Shuttleworth, J., Dorée, M., and Cavadore, J.C. (1993). The MO15 gene encodes the catalytic subunit of a protein kinase that activates cdc2 and other cyclin-dependent kinases (CDKs) through phosphorylation of Thr161 and its homologues. *EMBO J.* **12**, 3111–3121.

Fisher, R.P. (2005). Secrets of a double agent: CDK7 in cell-cycle control and transcription. *J. Cell Sci.* **118**, 5171–5180.

Fisher, R.P., and Morgan, D.O. (1994). A novel cyclin associates with MO15/CDK7 to form the CDK-activating kinase. *Cell* **78**, 713–724.

Gough, D.R., and Cotter, T.G. (2011). Hydrogen peroxide: a Jekyll and Hyde signalling molecule. *Cell Death Dis.* **2**, e213.

Gould, K.L., Moreno, S., Owen, D.J., Sazer, S., and Nurse, P. (1991). Phosphorylation at Thr167 is required for Schizosaccharomyces pombe p34cdc2 function. *EMBO J.* **10**, 3297–3309.

Gupta, V., and Carroll, K.S. (2016). Profiling the reactivity of cyclic C-nucleophiles towards electrophilic sulfur in cysteine sulfenic acid. *Chem. Sci.* **7**, 400–415.

Gupta, V., Yang, J., Liebler, D.C., and Carroll, K.S. (2017). Diverse Redoxome reactivity profiles of carbon nucleophiles. *J. Am. Chem. Soc.* **139**, 5588–5595.

Gurusamy, N., Mukherjee, S., Lekli, I., Bearzi, C., Bardelli, S., and Das, D.K. (2009). Inhibition of ref-1 stimulates the production of reactive oxygen species and induces differentiation in adult cardiac stem cells. *Antioxid. Redox Signal.* **11**, 589–600.

Gyuris, J., Golemis, E., Chertkov, H., and Brent, R. (1993). Cdi1, a human G1 and S phase protein phosphatase that associates with Cdk2. *Cell* **75**, 791–803.

Hannon, G.J., Casso, D., and Beach, D. (1994). KAP: a dual specificity phosphatase that interacts with cyclin-dependent kinases. *Proc. Natl. Acad. Sci. USA* **91**, 1731–1735.

Harper, J.W., and Elledge, S.J. (1998). The role of Cdk7 in CAK function, a retro-retrospective. *Genes Dev.* **12**, 285–289.

Havens, C.G., Ho, A., Yoshioka, N., and Dowdy, S.F. (2006). Regulation of late G1/S phase transition and APC Cdh1 by reactive oxygen species. *Mol. Cell Biol.* **26**, 4701–4711.

Holmström, K.M., and Finkel, T. (2014). Cellular mechanisms and physiological consequences of redox-dependent signalling. *Nat. Rev. Mol. Cell Biol.* **15**, 411–421.

Irani, K., Xia, Y., Zweier, J.L., Sollott, S.J., Der, C.J., Fearon, E.R., Sundaresan, M., Finkel, T., and Goldschmidt-Clermont, P.J. (1997). Mitogenic signaling

mediated by oxidants in Ras-transformed fibroblasts. *Science* 275, 1649–1652.

Ivanova, J.S., Pugovkina, N.A., Neganova, I.E., Kozhukharova, I.V., Nikolsky, N.N., and Lyublinskaya, O.G. (2021). Cell cycle-coupled changes in the level of reactive oxygen species support the proliferation of human pluripotent stem cells. *Stem Cells Dayt. Ohio* 39, 1671–1687.

Jones, R.G., Plas, D.R., Kubek, S., Buzzai, M., Mu, J., Xu, Y., Birnbaum, M.J., and Thompson, C.B. (2005). AMP-activated protein kinase induces a p53-dependent metabolic checkpoint. *Mol. Cell* 18, 283–293.

Kalyanaraman, B., Darley-Usmar, V., Davies, K.J., Dennery, P.A., Forman, H.J., Grisham, M.B., Mann, G.E., Moore, K., Roberts, L.J., and Ischiropoulos, H. (2012). Measuring reactive oxygen and nitrogen species with fluorescent probes: challenges and limitations. *Free Radic. Biol. Med.* 52, 1–6.

Kardash, E., Bandemer, J., and Raz, E. (2011). Imaging protein activity in live embryos using fluorescence resonance energy transfer biosensors. *Nat. Protoc.* 6, 1835–1846.

Kim, K.Y., Rhim, T., Choi, I., and Kim, S.S. (2001). N-acetylcysteine induces cell cycle arrest in hepatic stellate cells through its reducing activity. *J. Biol. Chem.* 276, 40591–40598.

Kyaw, M., Yoshizumi, M., Tsuchiya, K., Izawa, Y., Kanematsu, Y., Fujita, Y., Ali, N., Ishizawa, K., Yamauchi, A., and Tamaki, T. (2004). Antioxidant effects of stereoisomers of N-acetylcysteine (NAC), L-NAC and D-NAC, on angiotensin II-stimulated MAP kinase activation and vascular smooth muscle cell proliferation. *J. Pharmacol. Sci.* 95, 483–486.

Larochelle, S., Merrick, K.A., Terret, M.E., Wohlbold, L., Barboza, N.M., Zhang, C., Shokat, K.M., Jallepalli, P.V., and Fisher, R.P. (2007). Requirements for Cdk7 in the assembly of Cdk1/cyclin B and activation of Cdk2 revealed by chemical genetics in human cells. *Mol. Cell* 25, 839–850.

Lee, Y.-H., and Chu, W.-S. (1996). D-amino acid oxidase activity from *Rhodospiridium toruloides*. *Lett. Appl. Microbiol.* 23, 283–286.

Leonhardt, H., Rahn, H.P., Weinzierl, P., Sporbert, A., Cremer, T., Zink, D., and Cardoso, M.C. (2000). Dynamics of DNA replication factories in living cells. *J. Cell Biol.* 149, 271–280.

Mäkelä, T.P., Tassan, J.P., Nigg, E.A., Frutiger, S., Hughes, G.J., and Weinberg, R.A. (1994). A cyclin associated with the CDK-activating kinase MO15. *Nature* 371, 254–257.

Mandal, S., Guptan, P., Owusu-Ansah, E., and Banerjee, U. (2005). Mitochondrial regulation of cell cycle progression during development as revealed by the tenured mutation in *Drosophila*. *Dev. Cell* 9, 843–854.

Matlashov, M.E., Belousov, V.V., and Enikolopov, G. (2014). How much H₂O₂ is produced by recombinant D-amino acid oxidase in mammalian cells? *Antioxid. Redox Signal.* 20, 1039–1044.

Menon, S.G., and Goswami, P.C. (2007). A redox cycle within the cell cycle: ring in the old with the new. *Oncogene* 26, 1101–1109.

Menon, S.G., Sarsour, E.H., Kalen, A.L., Venkataraman, S., Hitchler, M.J., Domann, F.E., Oberley, L.W., and Goswami, P.C. (2007). Superoxide signaling mediates N-acetyl-L-cysteine-induced G1 arrest: regulatory role of cyclin D1 and manganese superoxide dismutase. *Cancer Res.* 67, 6392–6399.

Merrick, K.A., Larochelle, S., Zhang, C., Allen, J.J., Shokat, K.M., and Fisher, R.P. (2008). Distinct activation pathways confer cyclin-binding specificity on Cdk1 and Cdk2 in human cells. *Mol. Cell* 32, 662–672.

Merrick, K.A., Wohlbold, L., Zhang, C., Allen, J.J., Horiuchi, D., Huskey, N.E., Goga, A., Shokat, K.M., and Fisher, R.P. (2011). Switching Cdk2 on or off with small molecules to reveal requirements in human cell proliferation. *Mol. Cell* 42, 624–636.

Mitra, K., Wunder, C., Roysam, B., Lin, G., and Lippincott-Schwartz, J. (2009). A hyperfused mitochondrial state achieved at G1-S regulates cyclin E buildup and entry into S phase. *Proc. Natl. Acad. Sci. USA* 106, 11960–11965.

Moll, F., Walter, M., Rezende, F., Helfinger, V., Vasconez, E., De Oliveira, T., Greten, F.R., Olesch, C., Weigert, A., Radeke, H.H., et al. (2018). NoxO1 controls proliferation of colon epithelial cells. *Front. Immunol.* 9, 973.

Möller, M.N., Cuevasanta, E., Orrico, F., Lopez, A.C., Thomson, L., and Denicola, A. (2019). Diffusion and transport of reactive species Across cell membranes. *Adv. Exp. Med. Biol.* 1127, 3–19.

Morgan, D.O. (2007). *The Cell Cycle: Principles of Control* (New Science Press).

Murphy, M.P. (2009). How mitochondria produce reactive oxygen species. *Biochem. J.* 417, 1–13.

Murrell, G.A., Francis, M.J., and Bromley, L. (1990). Modulation of fibroblast proliferation by oxygen free radicals. *Biochem. J.* 265, 659–665.

Ogrunc, M., Di Micco, R., Liontos, M., Bombardelli, L., Mione, M., Fumagalli, M., Gorgoulis, V.G., and d’Adda di Fagagna, F. (2014). Oncogene-induced reactive oxygen species fuel hyperproliferation and DNA damage response activation. *Cell Death Differ.* 21, 998–1012.

Oh, E., Mark, K.G., Mocciaro, A., Watson, E.R., Prabu, J.R., Cha, D.D., Kampmann, M., Gamarra, N., Zhou, C.Y., and Rape, M. (2020). Gene expression and cell identity controlled by anaphase-promoting complex. *Nature* 579, 136–140.

Ohguro, N., Fukuda, M., Sasabe, T., and Tano, Y. (1999). Concentration dependent effects of hydrogen peroxide on lens epithelial cells. *Br. J. Ophthalmol.* 83, 1064–1068.

Owusu-Ansah, E., Yavari, A., Mandal, S., and Banerjee, U. (2008). Distinct mitochondrial retrograde signals control the G1-S cell cycle checkpoint. *Nat. Genet.* 40, 356–361.

Pak, V.V., Ezeriņa, D., Lyublinskaya, O.G., Pedre, B., Tyurin-Kuzmin, P.A., Mishina, N.M., Thauvin, M., Young, D., Wahni, K., Martínez Gache, S.A., et al. (2020). Ultrasensitive genetically encoded indicator for hydrogen peroxide identifies roles for the oxidant in cell migration and mitochondrial function. *Cell Metab.* 31, 642–653.e6.

Paul, M.K., Bisht, B., Darmawan, D.O., Chiou, R., Ha, V.L., Wallace, W.D., Chon, A.T., Hegab, A.E., Grogan, T., Elashoff, D.A., et al. (2014). Dynamic changes in intracellular ROS levels regulate airway basal stem cell homeostasis through Nrf2-dependent Notch signaling. *Cell Stem Cell* 15, 199–214.

Poon, R.Y., and Hunter, T. (1995). Dephosphorylation of Cdk2 Thr160 by the cyclin-dependent kinase-interacting phosphatase KAP in the absence of cyclin. *Science* 270, 90–93.

Poon, R.Y., Yamashita, K., Adamczewski, J.P., Hunt, T., and Shuttleworth, J. (1993). The cdc2-related protein p40MO15 is the catalytic subunit of a protein kinase that can activate p33cdk2 and p34cdc2. *EMBO J.* 12, 3123–3132.

Rapkin, L. (1931). A thiol cycle in dividing urchin eggs. *Ann. Physicochim. Biol.* 7, 382–386.

Reczek, C.R., and Chandel, N.S. (2017). The two faces of reactive oxygen species in cancer. *Annu. Rev. Cancer Biol.* 1, 79–98.

Reddie, K.G., and Carroll, K.S. (2008). Expanding the functional diversity of proteins through cysteine oxidation. *Curr. Opin. Chem. Biol.* 12, 746–754.

Robbins, E., and Morrill, G.A. (1969). Oxygen uptake during the HeLa cell life cycle and its correlation with macromolecular synthesis. *J. Cell Biol.* 43, 629–633.

Safford, S.E., Oberley, T.D., Urano, M., and St Clair, D.K. (1994). Suppression of fibrosarcoma metastasis by elevated expression of manganese superoxide dismutase. *Cancer Res.* 54, 4261–4265.

Sakaue-Sawano, A., Kurokawa, H., Morimura, T., Hanyu, A., Hama, H., Osawa, H., Kashiwagi, S., Fukami, K., Miyata, T., Miyoshi, H., et al. (2008). Visualizing spatiotemporal dynamics of multicellular cell-cycle progression. *Cell* 132, 487–498.

Sansam, C.G., Goins, D., Siefert, J.C., Clowdus, E.A., and Sansam, C.L. (2015). Cyclin-dependent kinase regulates the length of S phase through TICRR/TRESLIN phosphorylation. *Genes Dev.* 29, 555–566.

Schieber, M., and Chandel, N.S. (2014). ROS function in redox signaling and oxidative stress. *Curr. Biol.* 24, R453–R462.

Schindelin, J., Arganda-Carreras, I., Frise, E., Kaynig, V., Longair, M., Pietzsch, T., Preibisch, S., Rueden, C., Saalfeld, S., Schmid, B., et al. (2012). Fiji: an open-source platform for biological-image analysis. *Nat. Methods* 9, 676–682.

- Schmitz, M.H.A., and Gerlich, D.W. (2009). Automated live microscopy to study mitotic gene function in fluorescent reporter cell lines. *Methods Mol. Biol.* **545**, 113–134.
- Shadel, G.S., and Horvath, T.L. (2015). Mitochondrial ROS signaling in organismal homeostasis. *Cell* **163**, 560–569.
- Shi, Y., Fu, L., Yang, J., and Carroll, K.S. (2021). Wittig reagents for chemoselective sulfenic acid ligation enables global site stoichiometry analysis and redox-controlled mitochondrial targeting. *Nat. Chem.* **13**, 1140–1150.
- Sigaud, S., Evelson, P., and González-Flecha, B. (2005). H₂O₂-induced proliferation of primary alveolar epithelial cells is mediated by MAP kinases. *Antioxid. Redox Signal.* **7**, 6–13.
- Solomon, M.J., Harper, J.W., and Shuttleworth, J. (1993). CAK, the p34cdc2 activating kinase, contains a protein identical or closely related to p40MO15. *EMBO J.* **12**, 3133–3142.
- Song, H., Hanlon, N., Brown, N.R., Noble, M.E., Johnson, L.N., and Barford, D. (2001). Phosphoprotein-protein interactions revealed by the crystal structure of kinase-associated phosphatase in complex with phosphoCDK2. *Mol. Cell* **7**, 615–626.
- Spencer, S.L., Cappell, S.D., Tsai, F.C., Overton, K.W., Wang, C.L., and Meyer, T. (2013). The proliferation-quiescence decision is controlled by a bifurcation in CDK2 activity at mitotic exit. *Cell* **155**, 369–383.
- Sullivan, L.B., Gui, D.Y., Hosios, A.M., Bush, L.N., Freinkman, E., and Vander Heiden, M.G. (2015). Supporting aspartate biosynthesis is an essential function of respiration in proliferating cells. *Cell* **162**, 552–563.
- Trotter, E.W., and Hagan, I.M. (2020). Release from cell cycle arrest with Cdk4/6 inhibitors generates highly synchronized cell cycle progression in human cell culture. *Open Biol.* **10**, 200200.
- Tsai, C.C., Chen, Y.J., Yew, T.L., Chen, L.L., Wang, J.Y., Chiu, C.H., and Hung, S.C. (2011). Hypoxia inhibits senescence and maintains mesenchymal stem cell properties through down-regulation of E2A-p21 by HIF-TWIST. *Blood* **117**, 459–469.
- van den Heuvel, S., and Harlow, E. (1993). Distinct roles for cyclin-dependent kinases in cell cycle control. *Science* **262**, 2050–2054.
- Wagner, S., Thierbach, K., Zerjatke, T., Glauche, I., Roeder, I., and Scherf, N. (2021). TraCurate: efficiently curating cell tracks. *SoftwareX* **13**, 100656.
- Wang, Y., Branicky, R., Noë, A., and Hekimi, S. (2018). Superoxide dismutases: dual roles in controlling ROS damage and regulating ROS signaling. *J. Cell Biol.* **217**, 1915–1928.
- Wartenberg, M., Diedershagen, H., Hescheler, J., and Sauer, H. (1999). Growth stimulation versus induction of cell quiescence by hydrogen peroxide in prostate tumor spheroids is encoded by the duration of the Ca(2+) response. *J. Biol. Chem.* **274**, 27759–27767.
- Weinberg, F., Hamanaka, R., Wheaton, W.W., Weinberg, S., Joseph, J., Lopez, M., Kalyanaraman, B., Mutlu, G.M., Budinger, G.R., and Chandel, N.S. (2010). Mitochondrial metabolism and ROS generation are essential for Kras-mediated tumorigenicity. *Proc. Natl. Acad. Sci. USA* **107**, 8788–8793.
- Winterbourn, C.C. (2008). Reconciling the chemistry and biology of reactive oxygen species. *Nat. Chem. Biol.* **4**, 278–286.
- Xiao, H., Jedrychowski, M.P., Schweppe, D.K., Huttlin, E.L., Yu, Q., Heppner, D.E., Li, J., Long, J., Mills, E.L., Szpyt, J., et al. (2020). A quantitative tissue-specific landscape of protein redox regulation during. *Aging Cell* **180**, 968–983.e24.
- Yang, J., Gupta, V., Tallman, K.A., Porter, N.A., Carroll, K.S., and Liebler, D.C. (2015). Global, *in situ*, site-specific analysis of protein S-sulfenylation. *Nat. Protoc.* **10**, 1022–1037.
- Yeh, C.T., Lu, S.C., Chao, C.H., and Chao, M.L. (2003). Abolishment of the interaction between cyclin-dependent kinase 2 and Cdk-associated protein phosphatase by a truncated KAP mutant. *Biochem. Biophys. Res. Commun.* **305**, 311–314.
- Zerjatke, T., Gak, I.A., Kirova, D., Fuhrmann, M., Daniel, K., Gonciarz, M., Müller, D., Glauche, I., and Mansfeld, J. (2017). Quantitative cell cycle analysis based on an endogenous all-in-one reporter for cell tracking and classification. *Cell Rep.* **19**, 1953–1966.

STAR★METHODS

KEY RESOURCES TABLE

REAGENT or RESOURCE	SOURCE	IDENTIFIER
Antibodies		
CDK2	BD Bioscience	Cat# 610146; RRID: AB_397547
CDK2 pT160	Cell Signaling Technology	Cat# 2561; RRID: AB_2078685
CDK4	Cell Signaling Technology	Cat# 12790; RRID: AB_2631166
CDK7	Cell Signaling Technology	Cat# 2916; RRID: AB_2077142
CSE1	Abcam	Cat# ab54674; RRID: AB_940806
CSE1	Abcam	Cat# ab96755; RRID: AB_10865417
Cyclin A2	Santa Cruz	Cat# sc-596; RRID: AB_631330
Cyclin B1	BD Pharmingen	Cat# 554177; RRID: AB_395288
Cyclin E1	Bethyl	Cat# A301-566A; RRID: AB_1039994
eIF4G	Cell Signaling Technology	Cat# 2469; RRID: AB_2096028
GAPDH	Cell Signaling Technology	Cat# 2118; RRID: AB_561053
Geminin	Cell Signaling Technology	Cat# 5165; RRID: AB_10623289
KAP (CDKN3)	Abcam	Cat# ab175393
Mouse anti-HA Tag (YPYDVPDYA)	Custom-made	N/A
p21	Cell Signaling Technology	Cat# 2947; RRID: AB_823586
PARP	Cell Signaling Technology	Cat# 9542; RRID: AB_2160739
PDHA	GeneTex	Cat# GTX104015; RRID: AB_1951155
PDHB	GeneTex	Cat# GTX119625; RRID: AB_11163683
RPL26	Bethyl	Cat# A300-686A; RRID: AB_530289
Streptavidin	Abcam	Cat# ab76949; RRID: AB_1524455
α -tubulin	Sigma Aldrich	Cat# T5168; RRID: AB_477579
β -actin	Sigma Aldrich	Cat# A5441; RRID: AB_476744
IRDye 680RD Donkey anti-Rabbit IgG (H+L)	LI-COR Biosciences	Cat# 926-68073; RRID: AB_10954442
IRDye 800CW Donkey anti-Rabbit IgG (H + L)	LI-COR Biosciences	Cat# 926-32213; RRID: AB_621848
IRDye 800CW Donkey anti-Mouse IgG (H + L)	LI-COR Biosciences	Cat# 926-32212; RRID: AB_621847
IRDye 680RD Donkey anti-Rabbit IgG (H + L)	LI-COR Biosciences	Cat# 926-68073; RRID: AB_10954442
Anti-rabbit IgG, HRP-linked Antibody	Cell Signaling Technology	Cat# 7074; RRID: AB_2099233
Anti-mouse IgG, HRP-linked Antibody	Cell Signaling Technology	Cat# 7076; RRID: AB_330924
Anti-mouse IgG, HRP-linked Antibody	Cell Signaling Technology	Cat# 7076S; RRID: AB_330924
Virus strains		
AAV Helper-free System	Stratagene	Cat# 240071
Chemicals, peptides, and recombinant proteins		
6-Benzylaminopurine (6-BAP)	Sigma Aldrich	Cat# B3408
AF647-Picolyl-azide	Jena Biosciences	Cat# CLK-1300
Amphotericin B	Sigma Aldrich	Cat# A2942
AZDye 800 Picolyl Azide (Az800)	Click Chemistry Tools	Cat# 1563-5
Benzonase	Sigma Aldrich	Cat# E1014
Biotin	Sigma Aldrich	Cat# B4639
BSA (Fraction V)	Roth	Cat# 8076.4

(Continued on next page)

Continued

REAGENT or RESOURCE	SOURCE	IDENTIFIER
BTD	Kindly provided by Kate Carroll, Scripps, UF, USA and André Nadler, MPI-CBG Dresden, Germany	https://doi.org/10.1021/jacs.7b01791
CellRox Deep Red	Invitrogen	Cat# C10422
cOmplete™, EDTA-free Protease Inhibitor Cocktail	Merck	Cat# 4693132001
Copper(II) sulfate	Sigma Aldrich	Cat# C1297
D-alanine	Sigma Aldrich	Cat# A7377
DMSO	Sigma Aldrich	Cat# D2650
Dry milk powder	Roth	Cat# T145.3
DTT	Sigma Aldrich	Cat# D0632
Formaldehyde	Thermo Scientific	Cat# 28908
Gelantine	VWR	Cat# 1040700500
Glutamax	Gibco	Cat# 35050038
Glycerol	VWR	Cat# 24386.298
Hoechst 33342	Sigma Aldrich	Cat# 14533
Iodoacetamide (IAA)	Sigma Aldrich	Cat# A3221
IRDye 800CW Streptavidin	LI-COR Biosciences	Cat# 926-32230
L-alanine	Sigma Aldrich	Cat# A7469
Lambda Protein Phosphatase	New England Biolabs	Cat# PO753
MES running buffer (Bolt)	Invitrogen	Cat# B0002
MitoSOX	Invitrogen	Cat# M36008
MitoTEMPO	Sigma Aldrich	Cat# SML0737
MitoTracker Green	Invitrogen	Cat# M7514
MOPS SDS running buffer (Bolt)	Invitrogen	Cat# B0001
N-acetyl-L-cysteine	Sigma Aldrich	Cat# A7250
Neomycin (G418)	Sigma Aldrich	Cat# G8168
NuPage LDS sample buffer	Invitrogen	Cat# NP0007
OPTIMEM	Gibco	Cat# 31985047
Palbociclib	Sigma Aldrich	Cat# PZ0383
Paraformaldehyde (PFA)	Merck	Cat# 1.040005
PEG-Catalase	Sigma Aldrich	Cat# C4963
Penicillin-streptomycin	Sigma Aldrich	Cat# P0781
PhosSTOP	Merck	Cat# 4906837001
Picolyl-azide PEG4-biotin	Jena Biosciences	Cat# CLK-1167
PP1 Analog III (3MB-PP1)	Merck	Cat# 529582
Puromycin	Sigma Aldrich	Cat# P8833
Recombinant CAK	ThermoFisher Scientific	Cat# PV3868
Recombinant KAP	Sigma Aldrich	Cat# SRP5175
RNAiMAX	ThermoFisher Scientific	Cat# 13778150
SIR-DNA	Spirochrome	Cat# SC007
Sodium Azide	Sigma Aldrich	Cat# S2002
Sodium bicarbonate	Gibco	Cat# 25080094
Sodium L-ascorbate	Sigma Aldrich	Cat# A7631
Soy protein isolate	Amazon/Vitasyg	ASIN# B01FK8PROK
TCEP	Sigma Aldrich	Cat# C4706
Thymidine	Sigma Aldrich	Cat# T9250
Tris-[(1-benzyl-1H-1,2,3-triazol-4-yl)-methyl]-amin (TBTA)	Sigma Aldrich	Cat# 678937

(Continued on next page)

Continued

REAGENT or RESOURCE	SOURCE	IDENTIFIER
Triton X-100	Sigma Aldrich	Cat# T8787
Trypsin-EDTA solution 10x	Sigma Aldrich	Cat# 59418C
Tween 20	VWR	Cat# M147

Critical commercial assays

ADP/ATP ratio assay kit	Sigma Aldrich	Cat# MAK135-1KT
Click-iT Plus EdU Alexa Fluor 488 Imaging Kit	ThermoFisher Scientific	Cat# C10637
Luminata Forte Western HRP Substrate	Millipore	Cat# WBLUF0500
ProteoSilver stain kit	Sigma Aldrich	Cat# PROTSIL1
Super Signal West Femto Maximum Sensitivity Substrate	ThermoFisher Scientific	Cat# 34095

Experimental models: Cell lines

RPE-1	ATCC	RRID: CVCL_4388
RPE-1 FRT/TR	Kindly provided by Jon Pines, ICR London, UK	RRID: CVCL_VP32
BJ fibroblasts	ATCC	RRID: CVCL_3653
AAV-293	Stratagene	RRID: CVCL_6871
RPE-1 mRuby-PCNA, Histone3.1-mTurquoise2, CylinA2-mVenus	Our lab has developed	https://doi.org/10.1016/j.celrep.2017.05.022
RPE-1 FRT/TR mRuby-PCNA	Our lab has developed	https://doi.org/10.1016/j.celrep.2017.05.022
RPE-1 CDK2-as	Kindly provided by Robert Fisher, Icahn School of Medicine, New York, USA	https://doi.org/10.1016/j.molcel.2011.03.031
RPE-1 FRT/TR mRuby-PCNA, Histone3.1-iRFP	this study	Table S1: #5
RPE-1 FRT/TR mRuby-PCNA Histone3.1-iRFP, mAG-hGeminin (1-110)	this study	Table S1: #6
RPE-1 FRT/TR mRuby-PCNA, Histone3.1-mTurquoise2	this study	Table S1: #7
RPE-1 FRT/TR mRuby-PCNA, Histone3.1-mTurquoise2, Cdk2 sensor (DHB-Venus)	this study	Table S1: #8
RPE-1 FRT/TR CDK2 sensor (DHB-mCherry)	this study	Table S1: #9
RPE-1 FRT/TR Clover-hGeminin(1-110), Histone3.1-mTurquoise2, CDK2 sensor (DHB-mCherry)	this study	Table S1: #10
RPE-1 FRT/TR mRuby-PCNA + Histone 3.1-iRFP + Hyper2-DAO-NES	this study	Table S1: #11
RPE-1 FRT/TR Hyper2-DAO-NLS	this study	Table S1: #12
RPE-1 FRT/TR CDK2 sensor (DHB-mCherry), NLS-DAO-HyPer2	this study	Table S1: #13
RPE-1 FRT/TR Hyper2-DAO-NES	this study	Table S1: #14
RPE-1 FRT/TR CDK2 sensor (DHB-mCherry), NES-DAO-HyPer2	this study	Table S1: #15
RPE-1 FRT/TR mKO2-hCdt1(30-120), Clover-hGeminin(1-110)	this study	Table S1: #16
RPE-1 FRT/TR Hyper7 + mRuby-PCNA + Histone 3.1-iRFP	this study	Table S1: #17
RPE-1 CDK2-as + CDK2 WT + eGFP (pool of 5 independent clones)	this study	Table S1: #19

(Continued on next page)

Continued

REAGENT or RESOURCE	SOURCE	IDENTIFIER
RPE-1 CDK2-as + CDK2 C177S + mRuby (pool of 5 independent clones)	this study	Table S1: #20
RPE-1 FRT/TR CDK2-HA (WT)	this study	Table S1: #21
RPE-1 FRT/TR CDK2-HA (C177S)	this study	Table S1: #22
Oligonucleotides		
esi-PDHB	Eupheria	HU-04685-1
esi-CTRL (5'-TGCCCTTAAACACT CACTGGTCACGAGCGATACAATT CGCATACGGAGATAGGAGAATC GTCATACGTCGATACAGGTGCA TAAAACGGCCTTCCAAGATTGCGT CGATCTAATATTTTCGGGGGACG ATTAATATAAATGGGTCTTCTACA AGTCTATTGATCATAGTTCTTAAC GTAGGGACGTTCTTACATGAAA TAAGACTTAGTTACCACACTTCAA TATTCATTTTGCCCGACCTGTC GCCAG-3')	Eupheria	custom design
si-PDHA (5'-AGGUUGUGCUAA AGGGAAA-3')	Eurofins	custom design
si-CTRL (5'-UGGUUUACAUGU CGACUAA-3')	Eurofins	custom design
Oligonucleotides used for PCR and cloning	IDT, Sigma Aldrich	See Table S2
Recombinant DNA		
pAAV-Histone3.1-iRFP	this study	Table S2: #1
pcDNA3-mAG-Geminin (1/110)	N/A	https://doi.org/10.1016/j.cell.2007.12.033
pAAV-H3.1-mTurquoise2	Our lab has developed	https://doi.org/10.1016/j.celrep.2017.05.022
SCII-CDK2 sensor (Venus)	Kindly provided by Sabrina Spencer, University of Colorado, USA	https://doi.org/10.1016/j.cell.2013.08.062
pIRESNeomycin3-Cdk2-sensor (Venus)	this study	Table S2: #5
CAGGS-NLS-Flag-Cas9-IRES-Puromycin	Kindly provided by Francis Stewart, TU Dresden, Germany	https://doi.org/10.1038/srep25529
pIRES-EGFP	Clontech	6029-1
pIRESNeo3	Clontech	6988-1
pIRESNeomycin3-CAGGS promoter	this study	Table S2: #8
CSII-CDK2 sensor (DHB-mCherry)	Kindly provided by Sabrina Spencer, University of Colorado, USA	https://doi.org/10.1016/j.cell.2013.08.062
pIRESNeomycin3-CDK2 sensor (DHB-mCherry)	this study	Table S2: #10
pIRES-Puro3	Clontech	6986-1
pRIRESpuromycin3-CDK2 sensor (DHB-mCherry)	this study	Table S2: #12
pLL3.7m-Clover-Geminin(1-110)-IRES-mKO2-Cdt(30-120)	Addgene	RRID:Addgene_83841
pC1-HyPer-3	Addgene	RRID:Addgene_42131
pC1-Clover-Geminin(1-110)-IRES-mKO2-Cdt(30-120)	this study	Table S2: #15
pC1-Clover-Geminin(1-110)-IRES-Histone3.1-Turquoise2	this study	Table S2: #16
pAAV-Hyper2-DAO-NLS	Kindly provided Vsevolod Belousov, IBCh RAS, Russia	https://doi.org/10.1089/ars.2013.5618

(Continued on next page)

Continued

REAGENT or RESOURCE	SOURCE	IDENTIFIER
pCS2-HyPer7	Kindly provided Vsevolod Belousov, IBCh RAS, Russia	https://doi.org/10.1016/j.cmet.2020.02.003
pIRESNeomycin3-CDK2-StrepII-WT	this study	Table S2: #19
pIRESNeomycin3-CDK2-StrepII-C177S	this study	Table S2: #20
pIRESNeomycin3-CDK2-StrepII-C177A	this study	Table S2: #21
pIRESNeomycin3-Cdk6-StrepII-WT	this study	Table S2: #22
pAAV-Hyper2-DAO-NES	Kindly provided Vsevolod Belousov, IBCh RAS, Russia	https://doi.org/10.1089/ars.2013.5618
pMito-iRFP713	Addgene	RRID:Addgene_45465
pIRES2-CDK2(WT)-IRES2-eGFP	this study	Table S2: #25
pIRES2-CDK2(C177S)-IRES2-mRuby	this study	Table S2: #26
pDNA5 FRT/TO CDK2(WT)-HA	this study	Table S2: #27
pIRESNeomycin3_CDK2(C177S)-HA	this study	Table S2: #28
pIRESNeomycin3_CDK2(WT)-HA	this study	Table S2: #29
pIRESNeomycin3-CDK2(C177S)-HA	this study	Table S2: #30

Software and algorithms

Affinity Designer	Serif (Europe) Ltd	N/A
Fiji	N/A	https://doi.org/10.1038/nmeth.2019
FlowJo	Becton, Dickinson and Company	N/A
Mathematica 12.1	Wolfram Research Inc.	N/A
MetaXpress 5 and 6	Molecular Devices	N/A
Papers2	Mekentosj B.V.	N/A
Prism 6-9	Graph Pad	N/A
TraCurate	N/A	https://doi.org/10.1016/j.softx.2021.100656

Other

Auto-fluorescence-reduced imaging DMEM	Gibco	https://doi.org/10.1007/978-1-60327-993-2_7
DMEM	Gibco	41966052
DMEM/F12	Sigma Aldrich	D6421
Dynabeads Protein G	Invitrogen	10004D
Fetal Bovine Serum	Gibco	10500064
Fetal Bovine Serum, dialyzed	Gibco	26400044
Immobilon-FL PVDF	Millipore	IPFL00010
Leibovitz's L-15 Medium, no phenol red	Life Technologies	21083027
Minimum Essential Medium Eagle (MEM)	Sigma Aldrich	M2279
Magnetic streptavidin beads	Pierce	88816
MagStrep "type3" XT beads	IBA	2-4090-002

RESOURCE AVAILABILITY

Lead contact

Further information and requests should be directed to and will be fulfilled by the corresponding author: Dr. Jörg Mansfeld (jorg.mansfeld@icr.ac.uk)

Materials availability

Generated plasmids and cells are available from the [lead contact](#) upon request or have been deposited on Addgene.

Data and code availability

- This paper does not contain standardized datatypes. All other datatypes will be shared by the [lead contact](#) upon request.
- This paper does not report original code.

- Any additional information required to reanalyze the data reported in this paper is available from the [lead contact](#) upon request.

EXPERIMENTAL MODEL AND SUBJECT DETAILS

Cell lines and cell culture

All cell lines were cultured according to standard mammalian tissue culture protocol at 37 °C in 5% CO₂, assessed for authenticity by imaging, and tested for mycoplasma contamination. For hypoxia experiments, cells were adapted to 6.3% (RPE-1) and 4% O₂ (BJ) in Whitley H35 hypoxystation (Don Whitley Scientific) for 3–4 days before the experiment. Prior to imaging or flow cytometry analyses, cells were fixed at the indicated concentrations of O₂ in 3.7% PFA/PBS for 15 minutes. hTERT RPE-1 (Gender: female, RRID:CVCL_4388), hTERT RPE-1 FRT/TR (Gender: female, RRID:CVCL_VP32), hTERT-RPE-1 CDK2^{as} (Gender: female; [Merrick et al., 2011](#)) and the thereof derived cell lines listed in the [key resources table](#) and [Table S2](#) were grown in DMEM/F12 supplemented with 10% (v/v) FBS, 1% (v/v) penicillin-streptomycin, 1% (v/v) Glutamax, 0.5 μg/mL Amphotericin B and 0.26% sodium bicarbonate. AAV-293 (Gender: female, RRID:CVCL_6871) cells were grown in DMEM supplemented with 10% (v/v) FBS, 1% (v/v) penicillin-streptomycin, 1% (v/v) Glutamax, 0.5 μg/mL Amphotericin B. BJ fibroblasts (Gender: male, RRID:CVCL_3653) were grown in MEM supplemented with 10% FBS, 1% (v/v) penicillin-streptomycin and 1% (v/v) Glutamax. For BJ fibroblasts, the surface of cell culture plates was coated with 1% gelatin prior to seeding. Related to [Figures 1, 2, 3, 4, 5, 6, 7](#), and [S1–S3](#).

Plasmids and cell line generation

All plasmids and cell lines used in this study including vector backbones, PCR primers, templates, restriction sites, parent cell lines, inserts, methodology, and sources are listed in [Tables S1](#) and [S2](#). Gene knock-in of mRuby-PCNA and Histone 3.1-iRFP were created by rAAV-mediated gene targeting according to [Zerjatke et al. \(2017\)](#) and [Collin et al. \(2013\)](#). Stable cell lines were created by electroporation of plasmids using a Neon Transfection System (Thermo Fisher) according to the manufacturer's instructions. After 14–21 days, single positive clones were picked after selection with 400 μg/mL neomycin or 0.5 μg/mL puromycin. RPE-1 cell lines ectopically expressing HyPer2-DAO-NES or HyPer2-DAO-NLS were generated by viral transduction using an AAV gene targeting system (Stratagene) according to the manufacturer's instructions, and single HyPer2-fluorescent clones were selected by cell sorting on a BD FACSAria III (BD Biosciences). All cell lines used in this study including parental cell lines, plasmids, methods of creation, and references are described in [Table S1](#). For transient transfection, 8 μg of CDK2-StrepII WT or C177S plasmid were electroporated per 10⁶ cells, followed by extract preparation 48 hours later. Related to [Figures 1, 3, 5, 6, 7](#), and [S3](#).

METHOD DETAILS

Cell treatments

To synchronize RPE-1 cells at the beginning of S phase, 2.5 or 10 mM thymidine was added to the growth medium for 24 hours. To synchronize cells in G1 phase, 150 nM Palbociclib was supplied to media for 24 hours. For glutamine starvation experiments, cells were washed once with PBS, incubated for 6 hours in DMEM/F12 without glutamine and then supplemented with 10% (v/v) dialyzed FBS, 1% (v/v) penicillin-streptomycin, 0.5 μg/mL Amphotericin B, and 0.26% sodium bicarbonate. Stock solutions (500 mM) of N-acetyl-L-cysteine (NAC) in 7.5% sodium bicarbonate were always prepared freshly, adjusted with NaOH to pH 7.4–7.5, and added to cell culture media at the indicated concentrations and time. PEG-Catalase was dissolved in 50% glycerol/H₂O and added to the cells at the indicated amounts. Stock solutions (1 M) of D- and L-alanine in H₂O were stored at -20 °C and diluted to the indicated final concentration in growth media 24 hours after cell seeding for proliferation experiments ([Figure 1](#)) or 48 hours after esi-RNA transfection ([Figure 5](#)). MitoTEMPO was dissolved in DMSO and added at the indicated concentrations. Endogenous CDK2 in RPE-1 CDK2^{as} cells was inhibited by adding 10 μM 3MB-PP1 for the duration of the experiment. To ensure normal CDK-cyclin pairing ([Merrick et al., 2011](#)) 0.5 μM 6-benzylaminopurine (6-BAP) was added during cultivation and experiments as indicated. As a positive control for apoptosis ([Figure S1](#)) 50 μM sodium azide was added to RPE-1 cells for 24 hours. Related to [Figures 1, 4, 5, 6, 7](#), and [S1–S3](#).

RNA interference

esi-RNA or si-RNA oligonucleotides were delivered using RNAiMAX by reverse transfection according to the manufacturer's instructions. Briefly, transfections contained 16.5 ng esi-RNA per 96 well, 49.5 ng esi-RNA per μ-Slide 8 well, 1 μg esi-RNA per 6 well, or 50 nM of si-RNA mixed with 0.2 μL, 0.6 μL, and 2 μL of RNAiMAX in OPTIMEM, respectively. RNAi-treated cells were analyzed 48 hours after transfection with the exception of long-term time-lapse imaging ([Figures 3G](#) and [4A](#)), which was started already after 24 hours. Sequences for esi- and siRNAs are listed in the [key resources table](#). Related to [Figures 3, 4, 5, 6, S1](#), and [S2](#).

Proliferation experiments and EdU detection

To determine initial and final number of cells for proliferation experiments, complete 96 wells were imaged 5 hours after seeding (for esi/si-RNA experiments) or just prior to compound application and at the end of the experiment. Cell numbers were determined by detection and segmentation of nuclei using fluorescently tagged histone 3.1 or staining of DNA with 200 nM SIR-DNA (Spirochrome). For cell growth competition, RPE-1 CDK2^{as} cells stably expressing CDK2 WT and GFP from the same RNA (CDK2 WT_IRES2_eGFP) or CDK2 C177S and mRuby (CDK2 C177S_IRES2_mRuby) were seeded into the same 6 well in the presence of 10 μM 3MB-PP1. Cell

numbers of WT and C177S cells were determined by splitting $\sim 1,000 - 15,000$ cells from a 6 well into a 96 well plate, followed by incubation with 200 nM SIR-DNA and imaging 1 hour after seeding, when attachment of cells was complete. WT (GFP positive) and C177S (mRuby positive) cells were identified by single-cell analysis based on nuclear segmentation and GFP/mRuby detection using the segmentation and filter modules of MetaXpress Custom Module Editor (Molecular Devices). The ratio of WT/C177S cells on day 0 was set to 1 and the procedure was repeated on days 3 and 6. DNA replication was assessed by adding 10 μM EdU to cells for 45 minutes (Figures 4D and 4E) or the duration of the experiment (Figure 7N). Afterward, cells were fixed in 4% PFA/PBS for 15 minutes at RT, washed twice in 3% BSA/PBS and extracted for 20 minutes in 0.5% Triton X-100/PBS, followed by two 5 minutes washes in 3% BSA/PBS. Subsequently, EdU was labeled with Alexa 488 using a Click-iT Plus Edu Alexa Fluor 488 Imaging Kit according to the manufacturer's instructions (Figures 4D and 4E) or by the following protocol: a click mixture of PBS containing 4 mM CuSO₄, 5 mM AF647-Picolyl-azide and 10 mM sodium ascorbate was added to cells for 1 hour at RT in the dark (Figure 7N); after removal of the click mixture, cells were washed once in 3% BSA/PBS and PBS followed by staining of DNA with 2 μM Hoechst 33342 for 30 minutes, two washes with PBS, and image analysis. Related to Figures 4 and 7.

Lysate, extracts and interaction studies

To obtain total cell lysates, RPE-1 cells were washed once in PBS followed by the addition of 1x NuPAGE LDS Sample buffer containing 100 mM DTT. For extracts, cells were trypsinized with 2x Trypsin-EDTA, washed once in PBS, resuspended in extraction buffer P (30 mM Tris pH 7.5, 0.25% NP-40, 2.5 mM MgCl₂, 175 mM NaCl, 10% glycerol, 1 mM DTT, cOmplete protease inhibitors (Merck), phosSTOP phosphatase inhibitors (Merck), incubated for 20 minutes on ice and centrifuged at 13,000g for 15 minutes at 4°C. Cleared extracts were mixed 3:1 (v/v) with 3x NuPAGE LDS/DTT Sample buffer and boiled at 95°C for 5 minutes. For StrepII pull-downs RPE-1 cells were lysed with extraction buffer S (50 mM Tris pH 8, 150 mM NaCl, 2.5 mM MgCl₂, 5% glycerol, 1% Triton X-100), cOmplete protease inhibitors and incubated for 20 minutes on ice. Extracts were cleared (13,000g, 15 minutes, 4°C) and added to MagStrep "type3" XT beads equilibrated with extraction buffer and incubated for 30 minutes on a rotating wheel at 4°C. To assess binding of endogenous KAP to CDK2-StrepII-WT, living cells were incubated with 5 mM DTT at 37°C for 10 minutes prior to extraction in buffer S (-/+ 20 mM DTT). For analyses of CDK2 T160 phosphorylation, cyclin A2 binding, cyclin E1 binding and endogenous KAP, binding beads were washed 3x in extraction buffer S and precipitates were eluted in NuPAGE LDS/DTT sample buffer at 95°C for 5 minutes. For binding assays with recombinant GST-KAP or CAK, CDK2-WT-StrepII and CDK2-C177S-StrepII immobilized on MagStrep "type3" XT beads were washed 1x in extraction buffer S -/+ 10 mM DTT. For CAK binding assays CDK2 was dephosphorylated by washing beads once in λ -phosphatase buffer with 1 mM MnCl₂ and incubated with 400 units of λ phosphatase for 30 minutes at 4°C. Subsequently, CDK2 WT or C177S beads were incubated with or without 10 mM DTT in extraction buffer S including 0.1 $\mu\text{g}/\mu\text{L}$ bovine serum albumin (BSA) for 30 minutes at 4°C. KAP binding assays were performed for 30 minutes on a rotating wheel at 4°C with 60 ng KAP supplied to binding buffer K (50 mM Tris pH 6.8, 150 mM NaCl, 0.1 $\mu\text{g}/\mu\text{L}$ BSA) -/+ 1 mM DTT. CAK binding assays were performed for 1 hour on a rotating wheel at 4°C with 125 ng of CAK diluted in binding buffer C (8 mM MOPS/NaOH pH 7, 0.2 mM EDTA, 150 mM NaCl) -/+ 1 mM DTT. After binding, beads were washed twice with extraction buffer S and eluted with NuPAGE LDS/DTT sample buffer for 5 min at 95°C. For binding of endogenous KAP to CDK2-WT-StrepII, living cells were incubated with 5 mM DTT at 37°C for 10 minutes before extract preparation in buffer S -/+ 20 mM DTT. Staining of CDK2-StrepII pull-downs was performed using a ProteoSilver staining kit according to the manufacturer's instructions. Related to Figures 3, 4, 5, 6, 7, and S1-S3.

BTD labeling

RPE-1 cells were grown to 80-90% confluency in 15 cm dishes (Greiner Bio-One), washed once in PBS and labeled for sulfenic acids with 1 mM of the sulfenic acid-reactive probe BTM (Gupta et al., 2017). BTM stocks were dissolved in DMSO and added to the growth medium for 30 minutes at 37°C (0.5% final concentration DMSO). Subsequently, cells were washed twice with PBS and fixed in PBS/1% formaldehyde (FA) supplemented with 10 mM iodoacetamide (IAA) for 15 minutes. After further alkylation in PBS/10 mM IAA for 15 minutes, cells were reduced with 40 mM DTT/PBS for 30 minutes, washed once with PBS, permeabilized with 90% methanol at -20°C for 15 minutes, washed once with PBS and treated with 15 $\mu\text{g}/\text{mL}$ benzoyl peroxide per 15 cm dish for 15 minutes. After an additional wash in PBS, cells were blocked with PBS/5% BSA for 1 hour, washed once in PBS, and incubated with 0.5 nmol picolyl-azide PEG4-biotin in 7.5 mL PBS per dish. Clicking of biotin-azide to the alkene group of BTM was catalyzed by adding a 2x concentrated click mix to reach a final concentration of 1 mM CuSO₄, 0.1 mM Tris-[(1-benzyl-1H-1,2,3-triazol-4-yl)-methyl]-amin (TBTA) and 1 mM sodium ascorbate. After 1 hour clicking at RT, cells were washed once with PBS, thrice in PBS/0.1% Tween 20/10 mM EDTA for 10 minutes, once with PBS and scraped in 1 mL of PBS containing 2% SDS/5 mM DTT. Samples were then boiled at 95°C for 45 minutes to reverse the FA crosslink, cleared for 15 minutes at 13,000g, the supernatants diluted 6 times in PBS and incubated with PBS-equilibrated magnetic streptavidin beads on a wheel overnight at 4°C. Unbound material was removed, and beads were washed 4x in 4 M urea/0.5% SDS/25 mM HEPES, 4x in PBS/0.5% SDS and then transferred to a clean microfuge tube. After two more PBS washes, bound proteins were eluted by NuPAGE LDS sample buffer supplemented with 2.5 mM biotin/100 mM DTT at 95°C for 15 minutes (Figures 7B and S2J). To investigate the cell cycle-dependent oxidation of CDK2, RPE-1 cells expressing CDK2-HA WT were grown to 50% confluency and serum-starved for 24 hours. According to Figure S2I, cells were labeled at 8, 18 and 22 hours representing G1, S and G2 phases for 30 minutes at 37°C in media containing 1% FBS to minimize quenching of the BTM probe by FBS. Subsequently, cells were washed twice with PBS and lysed in 50 mM Tris pH 8, 400 mM NaCl, 5% glycerol, 1% SDS, supplemented with fresh 10 mM TCEP and cOmplete protease inhibitors for 15 minutes at RT. Lysates were alkylated with IAA (40 mM) for

15 minutes at RT in the dark and stored at -80°C until all time points were collected. Lysates were sonicated to shear DNA, cleared at $13,000 \times g$, and then a click reaction to conjugate BTD to Az800 (AZDye 800 Picolyl Azide) was performed as described above. Afterwards, proteins were precipitated by chloroform/methanol to remove click reagents and protein pellets were resuspended in 20 mM Tris pH 8, 0.5 M Urea and 0.5% SDS. Lysates were sonicated and diluted 1:7 with Buffer A containing 20 mM Tris pH 8, 120 mM NaCl and 1% Triton and incubated with protein G Dynabeads coupled to HA antibodies for 1 hour at 4°C . Beads were then washed once with Buffer A supplemented with 120 mM NaCl and thrice with Buffer A supplemented with 400 mM NaCl. CDK2-HA was eluted by boiling beads for 10 minutes at 65°C in NuPage LDS sample buffer, followed by transfer to a new tube, addition of 100 mM DTT and analysis by SDS-PAGE (Figures 7D and S3B). Related to Figures 7, S2, and S3.

SDS-PAGE and Western blot analyses

Proteins were separated by SDS-PAGE using Bis-Tris 4–12% Bolt gradient gels in MES or MOPS buffers in a Mini Gel Tank (Thermo Fisher). Western blot analyses were performed using a wet transfer Criterion Blotter (BioRad) in MOPS/20% ethanol transfer buffer using Immobilon-FL PVDF membranes. Membranes were blocked for 1 hour at RT in 5% dry milk or 5% soy protein isolate (for CDK2 pT160 detection) prepared in PBS/0.2% Tween 20. Primary antibodies were added overnight at 4°C , followed by 3x washing in PBS/0.02% Tween 20 and incubation with secondary antibodies for 1 hour at RT. For quantitative detection, fluorescently-labeled secondary antibodies were used with a near-infrared scanning system (Odyssey, Li-COR). Alternatively, detection was performed with horseradish peroxidase (HRP)-conjugated antibodies and Luminata Forte Western HRP Substrate or Super Signal West Femto Maximum Sensitivity Substrate on an ImageQuant LAS4000 system (Amersham Biosciences). Related to Figures 3, 4, 5, 6, 7, and S1–S3.

ROS labeling

For flow cytometry analyses by the LSR Fortessa FACS (BD Bioscience) analyzer, 10^6 asynchronous cells were labeled for 30 minutes with $5 \mu\text{g}/\text{mL}$ Hoechst 33342, trypsinized, washed in PBS and transferred to CO_2 -independent L15 medium supplemented with 10% FBS and 1% (v/v) penicillin-streptomycin, 1% (v/v) Glutamax, $0.5 \mu\text{g}/\text{mL}$ Amphotericin B and 0.26% sodium bicarbonate. Then, $5 \mu\text{g}/\text{mL}$ Hoechst 33342 and $5 \mu\text{M}$ CellRox Deep Red and/or MitoSox Red were added for 30 minutes or 100 nM MitoTracker Green for 10 minutes. ROS labeling of adherent cells was performed in living RPE-1 cells expressing endogenously tagged histone 3.1-Turquoise2, Ruby-PCNA, cyclinA2-Venus using the reagents, concentrations and labeling times indicated above, followed by a brief wash in PBS to remove the excess of the free dye and incubating cells in imaging DMEM (described below). The relative increase of cell volume versus mitochondria during the cell cycle was determined by forward scatter and MitoTracker Green, respectively, and normalized to the G1 population. Related to Figures 2 and S1.

ADP/ATP ratio

The ADP/ATP ratio was determined using an ADP/ATP ratio assay kit 48 hours after PDHB depletion in a 96 well plate. Measurements were performed according to the manufacturer's instructions on a Glomax Luminometer (Promega). Related to Figure 3.

Microscopy

Automated microscopy was performed on an ImageXpress Micro XLS wide-field screening microscope (Molecular Devices) equipped with 10x, 0.5 NA and 20x, 0.7 NA Plan Apo air objectives (Nikon) and laser-based autofocus. Excitation and detection were done by a Spectra X light engine (Lumencor) and sCMOS (Andor) camera with the indicated filters: DAPI (Ex: 377/50; Dic: 344-404 / 415-570; Em: 447/60); CFP (Ex: 438/24; Dic: 426-450/467-600; Em: 483/32); GFP (Ex: 472/30; Dic: 442-488 / 502-730; Em: 520/35), YFP (Ex: 513/17; Dic: 488-512 / 528-625; Em: 542/27), TexasRed (Ex: 575/25 Dic: 530-585 / 601-800; Em: 624/40) and Cy5 (Ex: 628/40; Dic: 594-651 / 669-726; Em: 692/40). During experiments, cells were maintained in a stage incubator at 37°C in a humidified atmosphere of 5% CO_2 . All cells were grown in black 96 well clear-bottom plates (μ clear, Greiner Bio-One). For long-term time-lapse microscopy and ROS imaging, the growth media was exchanged to an auto-fluorescence-reduced imaging DMEM (Schmitz and Gerlich, 2009) supplemented with 10% (v/v) FBS, 1% (v/v) penicillin-streptomycin, 1% Glutamax, $0.5 \mu\text{g}/\text{mL}$ Amphotericin B and 0.26% sodium bicarbonate. Long-term time-lapse microscopy was performed by taking images using a 10x objective at 7 minutes intervals for 48 hours. To determine the initial and final number of cells for proliferation experiments, the complete 96 well was imaged 5 hours after seeding (for esi/si-RNA experiments) or just prior to compound application and at the end of the experiment. Microscopy of cells stained with ROS-sensitive dyes was performed by acquiring maximum image projection using a 20x objective. For ratio imaging of HyPer2-DAO-NLS and HyPer2-DAO-NES cells with ImageXpress Micro XLS, the following filter sets were used: Ex: (438/24) with Em: (542/27), and Ex: (513/17) with Em: (542/27). For CDK2 sensor imaging of cells grown under physiological $\% \text{O}_2$, cells were fixed in 3.7% PFA/PBS before exposure to atmospheric O_2 . For ratio imaging to assess differences in ROS content between esi-CTRL and esi-PDHB treatments in HyPer 7-expressing cells, a Delta Vision Core wide-field deconvolution fluorescence microscope equipped with a CoolSNAP HQ2/HQ2-ICX285 camera (Applied Precision Inc.) and a UPlanSApo 40X/NA 0.95 lens (Olympus) was used. Cells were imaged using the following filters: Ex: (381-401) with Em: (500-523) and Ex: (464-492) with Em: (500-523). Related to Figures 1, 2, 3, 4, 5, 6, 7, S1, and S2.

QUANTIFICATION AND STATISTICAL ANALYSIS

Image analysis

Image analyses of single time points were performed in MetaXpress 5 and 6 (Molecular Devices) using customized image analysis pipelines. Briefly, images were flat-field and background corrected using a tophat filter and nuclei were segmented based on DNA or Ruby-PCNA labeling to create masks for fluorescence extraction. To determine the initial and final number of cells in proliferation experiments, the complete 96 well was imaged 5 hours after seeding (for esi/si-RNA experiments) or prior to compound application and again at the end of the experiment. Detection of PCNA replication foci was performed using the nuclear speckle plugin from the MetaXpress Custom Module Editor. Fucci analysis was performed by segmenting all nuclei based on SIR-DNA staining and by merging the nuclear intensities of Gem(1-110) and Cdt(30-120) to a common segmentation mask. Gem(1-110)- and Cdt(30-120)-positive cells were assigned by minimum threshold filtering and the cell cycle distribution was indicated as a fraction of the sum of Gem(1-110)- or Cdt(30-120)-positive cells (Figure S2C). Time-lapse analysis of single cells was performed as previously described (Zerjatke et al., 2017). Briefly, all images were background corrected using flat-field correction, and nuclei were segmented based on histone 3.1 labeling using intensity thresholding and subsequent watershed filtering. Time-lapse single-cell tracking was performed with a nearest-neighbor approach and subsequent manual track curation using TraCurate (Wagner et al., 2021). Cell cycle phases were classified according to PCNA mean intensity and distribution as described in Zerjatke et al. (2017). Nuclear CDK2 levels were quantified as mean intensities based on the histone segmentation masks. Cytoplasmic CDK2 levels were quantified as the mean intensities in two cap regions adjacent to the poles of each cell nuclei. Image analysis and quantification were performed with Mathematica 12.1 (Wolfram Research Inc.). Thresholds for CDK2^{Low}/CDK2^{High} cells were determined by histogram analysis of ratios of nuclear and cytoplasmic CDK2 to identify the CDK2^{Low} peak (Spencer et al., 2013). Ratio image analyses were performed in Fiji (Schindelin et al., 2012) using the Ratio Plus plugin as previously described (Kardash et al., 2011). Ratio image analyses of HyPer7 images were performed using a semi-automated Fiji macro. Briefly, the images were background corrected (rolling ball = 50), smoothed and a mask was defined based on the HyPer7 Ex: (464-492)/Em: (500-523) image and binarized. Then, images from both excitations were multiplied with the mask to remove background, converted to 32 bit, and the ratio image was calculated by dividing the HyPer 7 signal from (Ex: 464-492)/(Em: 500-523) by (Ex: 381-401)/Em: (500-523). Flow cytometry analyses were performed in FlowJo (Becton, Dickinson and Company). Forward scatter values were used as a relative proxy for cell size. Related to Figures 1, 3, 4, 5, 6, 7, S1, and S2.

Statistical methods

Data normalization was performed in Microsoft Excel (Microsoft), and statistical analysis and graph presentation were performed in Prism 6-9 (GraphPad) using the statistical tests indicated in the figure legends. All data are representative of at least three independent repeats unless otherwise stated. The notation n refers to the number of independently performed experiments, and the notation N refers to the number of data points used for statistical analyses and data presentation. A p-value lower than 0.05 was considered statistically significant and individual p-values are indicated in each figure or figure legend. Bar charts indicate the mean \pm SD and show all data points for N<10. Box plots show the median and 25th-75th percentiles, and whiskers represent the 5th-95th percentiles. For quantitative Western blot analyses by near-infrared fluorescence detection (Li-COR), band intensities were divided by the intensity of the loading control or total CDK2 levels (for pT160) to correct for sample loading. Time-lapse data of single-cell ratio imaging were smoothed with the 4 neighbors on each side and a 6th order polynomial using Prism 6. For flow cytometry analyses, the intensities of individual cell cycle phases were normalized by the sum of intensities of all cell cycle phases to correct for differences in overall staining intensities between experiments. No randomization or blinding was performed in this study. Related to Figures 1, 2, 3, 4, 5, 6, 7, and S1-S3.

Developmental Cell, Volume 57

Supplemental information

**A ROS-dependent mechanism
promotes CDK2 phosphorylation
to drive progression through S phase**

Dilyana Georgieva Kirova, Kristyna Judasova, Julia Vorhauser, Thomas Zerjatke, Jacky Kieran Leung, Ingmar Glauche, and Jörg Mansfeld

Figure S1

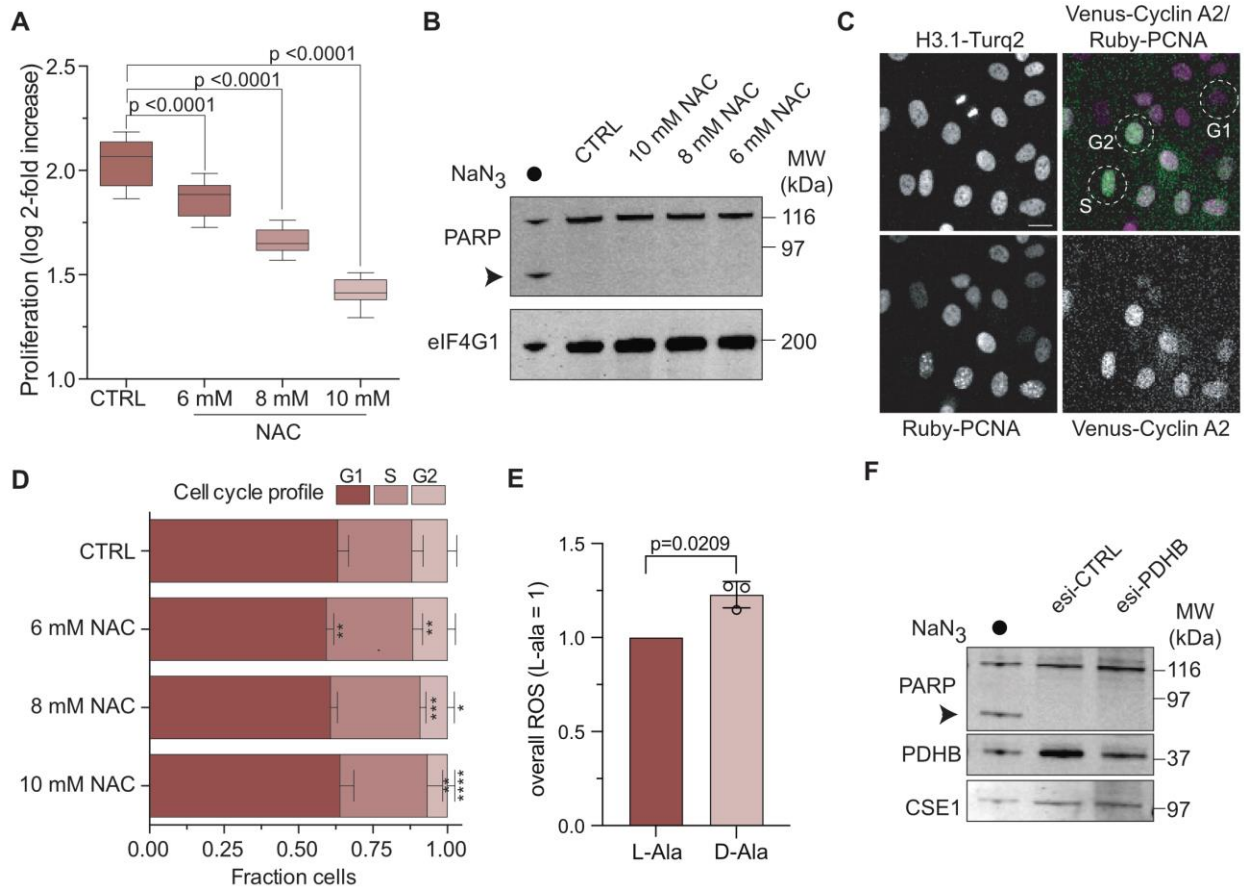


Figure S1, related to Figure 1 and Figure 3. Interference with ROS slows cell proliferation and does not induce apoptosis. (A) Proliferation of RPE-1 cells in the presence of NAC. Boxplots indicate the median log₂-fold proliferation of cells for 48 hours. Significance according to one-way ANOVA with Dunnett's multi comparison test (n=3, N=18). (B) Western blot analysis detecting PARP cleavage in cells treated with NAC or 50 μ M sodium azide (NaN₃) as a positive control. (C) Cell cycle analysis based on fluorescent markers. Cyclin A2-Venus negative cells are in G1 phase, cyclin A2-Venus positive cells are in S or G2 phase, and PCNA foci identify S phase. Circles in the overlay indicate examples of cells in G1, S and G2 phase, classified according to the expression of cyclin A2-Venus and PCNA foci. Scale bar = 10 μ m. (D) Stacked bars indicate the mean \pm SD fraction of the cells from (A) in cell cycle phases based on classification from (C). Significance according to one-way ANOVA with Holm-Sidak's multiple comparisons test: ** (6 mM NAC (G1) = 0.0077), ** (6 mM NAC (S) = 0.0085), *** (8 mM NAC (S) = 0.0007), * (8 mM NAC (G2) = 0.0133), ** (10 mM NAC (S) = 0.0046), **** (10 mM NAC (G2) = p<0.0001), (n=3, N=18). (E) Quantification of ROS detected by CellRox Deep Red in HyPer2-DAO-NES expressing RPE-1 cells in Figure 1F in response to 0.5 mM D-alanine (D-ala). Control cells were treated either with 0.5 mM or 5 mM L-alanine (L-ala). Bars represent the mean \pm SD. Significance according to two-tailed one-sample t-test (n=3, N=3). (F) Western blot analysis assessing PARP cleavage in cells depleted of PDHB.

Figure S2

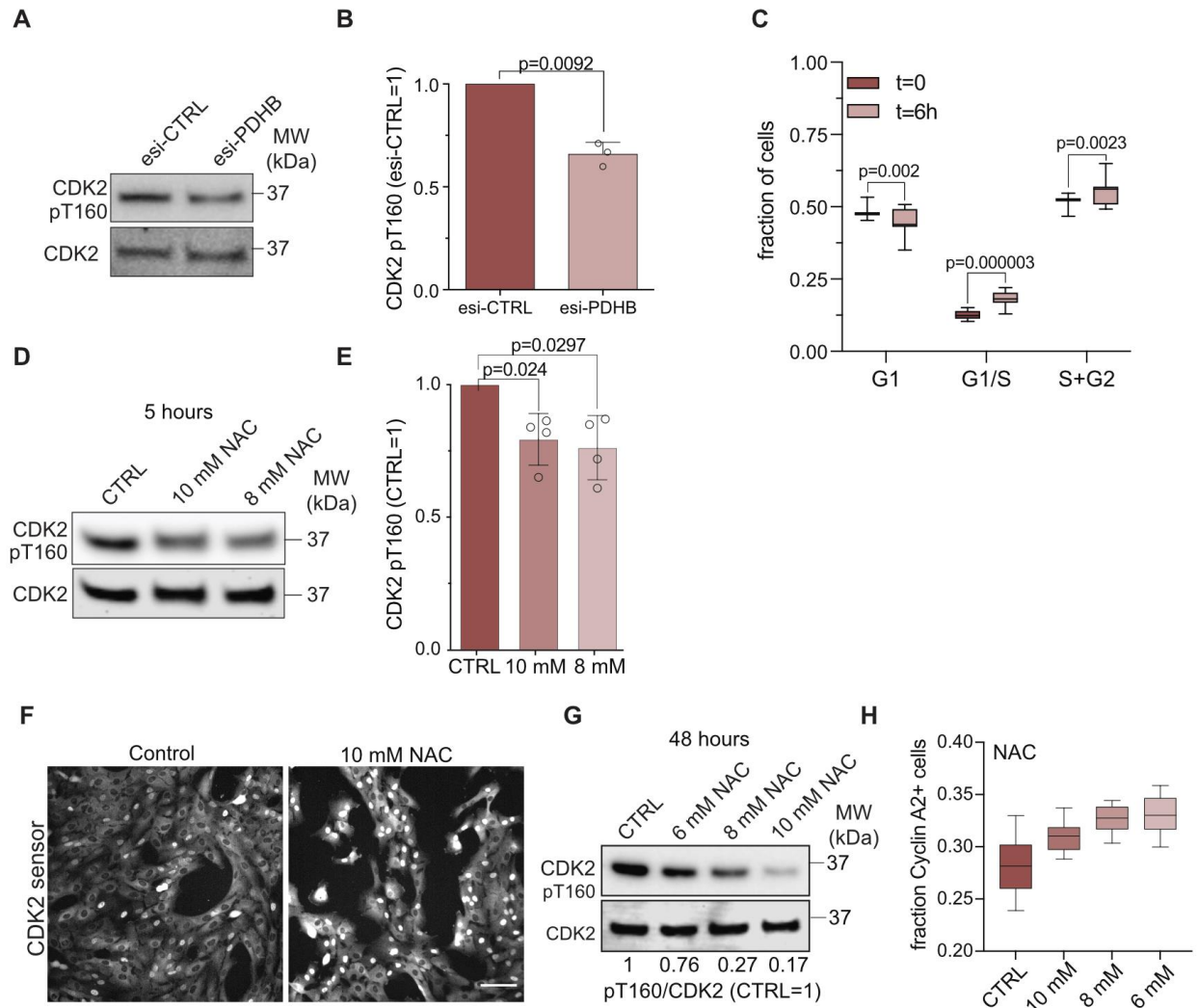


Figure S2, related to Figure 5. Changes in CDK2 T-loop phosphorylation in response to reductive treatments. (A) Western blot analysis showing T160 phosphorylation (pT160) in S phase synchronized RPE-1 cells depleted of PDHB for 48 hours. (B) Quantification of the data shown in (A). Bars indicate the mean \pm SD. Significance according to two-tailed one-sample t-test ($n=3$, $N=3$). (C) Cell cycle distribution analysis based on live cell imaging of Fucci-Gem and Fucci-Cdt expressing cells. Boxplots indicate the median fraction of cells in the indicated cell cycle phase at the beginning and after 6 hours of glutamine starvation. Significance according to two-way ANOVA with Sidak's multiple comparisons test ($n=3$, $N=18$). (D) Western blot analysis showing pT160 in S phase-synchronized RPE-1 cells 5 hours after treatment with NAC. (E) Quantification of the data shown in (D). Bars indicate the mean \pm SD. Significance according to two-tailed one-sample t-test ($n=4$, $N=4$). (F) Localization of CDK2 sensor 48 hours after treatment with NAC in RPE-1 cells. Scale bar = 100 μ m. (G) Western blot analysis ($n=2$) detecting pT160 in RPE-1 cells treated with NAC for 48 hours. (H) Single-cell analysis of Cyclin A2-Venus expressing cells treated as in (G). Boxplots indicate the median fraction of Cyclin A2 positive cells in response to NAC ($n=3$, $N=18$).

Figure S3

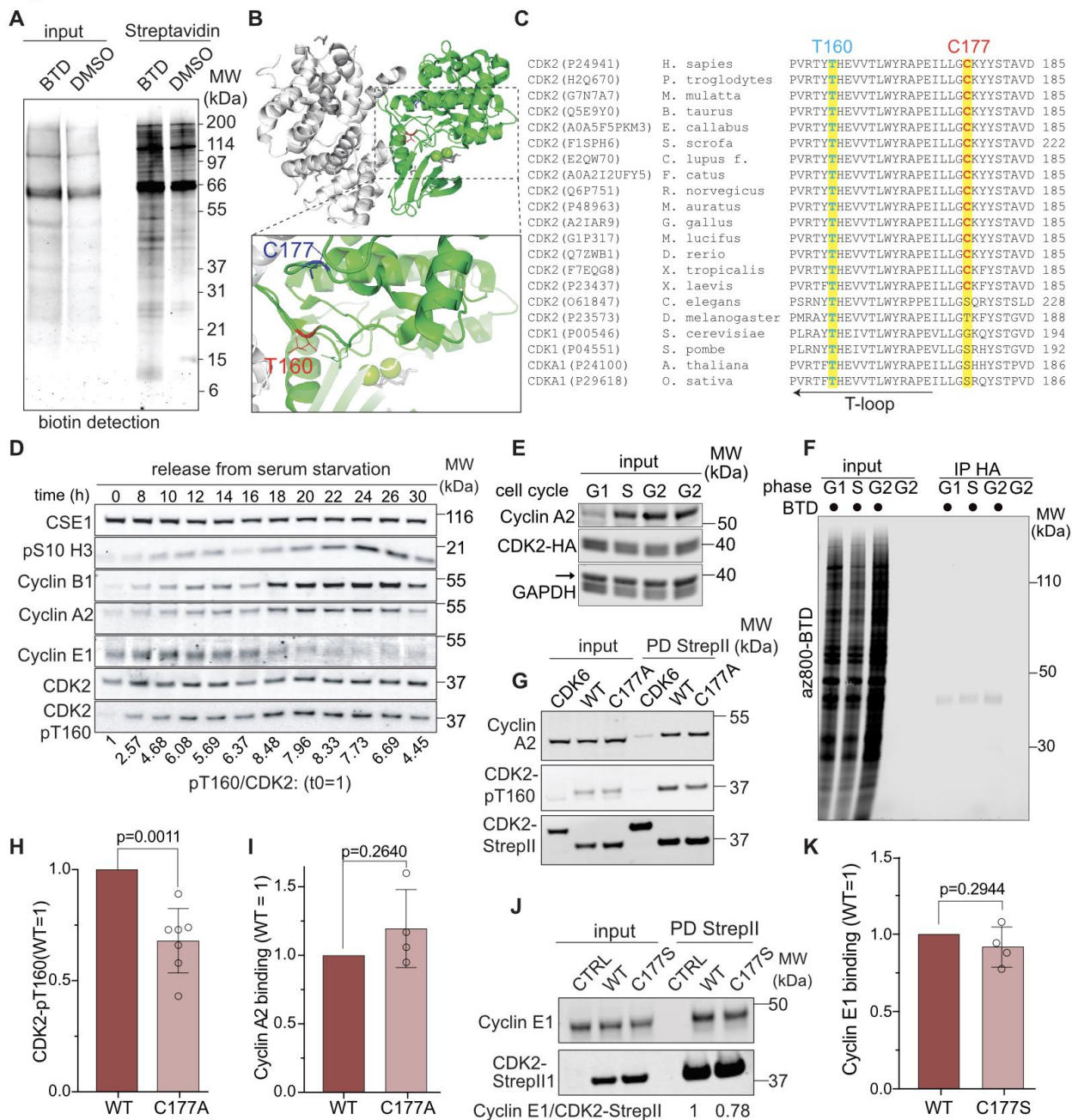


Figure S3, related to Figure 7. CDK2 oxidation during the cell cycle and C177 mutagenesis decrease T160 phosphorylation. (A) Biotin detection of Western Blot analysis in Figure 7B showing all BTD-biotin labeled proteins. (B) Structure of CDK2-cyclin A (PDB: 4I3Z) highlighting T160 (red) and C177 (blue). (C) Clustal Omega alignment of CDK2 kinases showing that C177 is highly conserved in vertebrates. Organisms in which CDK2 functions are exerted by a single CDK (i.e., in yeast or plants) do not contain a corresponding cysteine residue. (D) Western blot analysis (n=2) showing T-loop phosphorylation and expression of cell cycle markers in RPE-1 cells after releasing from 24h of serum starvation. The ratio of

phosphorylated T160 (pT160) to CDK2 normalized to t=0 is indicated beneath the Western blot. (E) Western blot analysis of the input samples of (F) and data shown in Figure 7D detecting the differential expression of cyclin A2 in G1 versus S and G2 phase samples. (F) Complete scan of the data presented in Figure 7D at a lower intensity to highlight differential BTB labeling of input samples at different stages of the cell cycle. (G-I) Western blot analysis and quantification of StrepII pull-downs using S-phase synchronized RPE-1 cells transiently expressing CDK2-WT-StrepII (WT) or CDK2-C177A-StrepII (C177A) or CDK6-StrepII as a control. Bars represent the mean \pm SD of pT160 and cyclin A2. Significance according to two-tailed one-sample t-test. (pT160: n=7, N=7; cyclin A2: n=4, N=4). (J-K) Western blot analysis and quantification of StrepII pull-downs using S-phase synchronized RPE-1 cells transiently expressing CDK2-WT-StrepII (WT) or CDK2-C177S-StrepII (C177S). Bars represent the mean \pm SD of Cyclin E1 binding. Significance according to two-tailed one-sample t-test. (n=4, N=4).

Figure S4

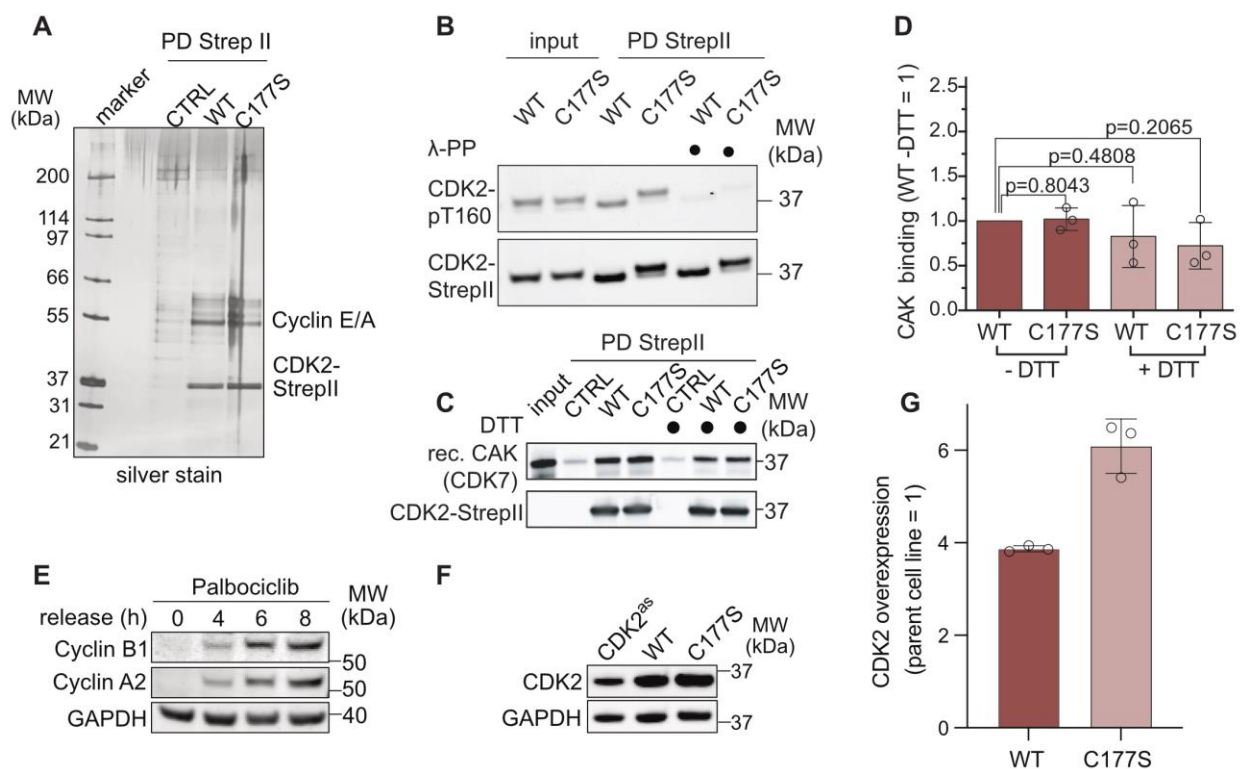


Figure S4, related to Figure 7. CDK2-CAK binding assays and rescue of RPE-1 CDK2^{as} cells with CDK2 WT and C177S. (A-C) Silver staining and Western blot analysis of Strep II pull-downs of CDK2 WT and C177S from lysates of S phase synchronized cells in the absence of DTT. Note, beads-bound CDK2-StrepII was used as shown in Figure 7H and for λ -phosphatase (λ -PP) treatment (B) and subsequent binding assays with recombinant CAK in the presence or absence of DTT (C). (D) Quantification of CAK binding to CDK2-StrepII from (C). Bars represent the mean \pm SD. Significance according to two-tailed unpaired one-sample t-test. (CAK: n=3, N=3). (E) Western blot analysis (n=2) of total lysates from RPE-1 cells released from a 24-hour Palbociclib block for 4 and 6 hours (as in Figure 7N), corresponding to early and mid S phase. (F) Western blot analysis of total lysates prepared from parent CDK2^{as} cells and CDK2^{as} cells stably expressing untagged CDK2 WT or C177S. (G) Quantification of CDK2 WT and C177S expression shown in (F) normalized to endogenous CDK2 levels in parental RPE-1 CDK2^{as} cells. Bars represent the mean and \pm SD. (n=3, N=3).

Supplemental Table 1. Generation of cell lines, related to STAR Methods.

No.	Name	Plasmid used	Parental cell line	Insert	Method	Reference
1	RPE-1	NA	NA	NA	NA	RRID:CVCL_4388
2	RPE-1 FRT/TR	NA	NA	NA	NA	RRID:CVCL_VP32
3	RPE-1 mRuby-PCNA, Histone3.1-mTurquoise2, CylinA2-mVenus	NA	NA	NA	NA	PMID: 28564611
4	RPE-1 FRT/TR mRuby-PCNA	NA	NA	NA	NA	PMID: 28564611
5	RPE-1 FRT/TR mRuby-PCNA, Histone3.1-iRFP	1	4	Histone3.1-iRFP	endogenous knock-in by rAAV gene-targeting	this study
6	RPE-1 FRT/TR mRuby-PCNA Histone3.1-iRFP, mAG-hGeminin (1-110)	2	5	mAG-Geminin (1-110)	ectopic expression, electroporation	this study
7	RPE-1 FRT/TR mRuby-PCNA, Histone3.1-mTurquoise2	3	4	Histone 3.1-mTurquoise2	endogenous knock-in by rAAV gene-targeting	this study
8	RPE-1 FRT/TR mRuby-PCNA, Histone3.1-mTurquoise2, Cdk2 sensor (DHB-Venus)	5	7	CDK sensor (DHB-Venus)	ectopic expression, electroporation	this study
9	RPE-1 FRT/TR CDK2 sensor (DHB-mCherry)	13	1	CDK2 sensor (DHB-mCherry)	ectopic expression, electroporation	this study
10	RPE-1 FRT/TR Clover-hGeminin(1-110), Histone3.1-mTurquoise2, CDK2 sensor (DHB-mCherry)	17	9	Clover-hGeminin(1-110), Histone3.1-mTurquoise2	ectopic expression, electroporation	this study
11	RPE-1 FRT/TR mRuby-PCNA + Histone 3.1-iRFP + Hyper2-DAO-NES	18	5	HyPer2-DAO-NES	ectopic expression, viral transduction	this study
12	RPE-1 FRT/TR Hyper2-DAO-NLS	18	2	HyPer2-DAO-NLS	ectopic expression, viral transduction	this study
13	RPE-1 FRT/TR CDK2 sensor (DHB-mCherry), NLS-DAO-HyPer2	11	12	CDK2 sensor (DHB-mCherry)	ectopic expression, electroporation	this study
14	RPE-1 FRT/TR Hyper2-DAO-NES	24	2	NES-DAO-HyPer2	ectopic expression, viral transduction	this study
15	RPE-1 FRT/TR CDK2 sensor (DHB-mCherry), NES-DAO-HyPer2	11	14	CDK2 sensor (DHB-mCherry)	ectopic expression, electroporation	this study
16	RPE-1 FRT/TR mKO2-hCdt1(30-120), Clover-hGeminin(1-110)	16	2	mKO2-hCdt1(30-120), Clover-hGeminin(1-110)	ectopic expression, electroporation	this study
17	RPE-1 FRT/TR Hyper7 + mRuby-PCNA + Histone 3.1-iRFP	19	5	HyPer7	ectopic expression, electroporation	this study
18	RPE-1 CDK2-as	NA	NA	NA	NA	PMID: 21658603
19	RPE-1 CDK2-as + CDK2 WT + eGFP (pool of 5 independent clones)	26	18	CDK2-WT_IRES2_eGFP	ectopic expression, electroporation	this study
20	RPE-1 CDK2-as + CDK2 C177S + mRuby (pool of 5 independent clones)	27	18	CDK2-C177S_IRES2_mRuby	ectopic expression, electroporation	this study
21	RPE-1 FRT/TR CDK2-HA (WT)	28	2	CDK2-WT-HA	integration into single FRT site, electroporation	this study

22	RPE-1 FRT/TR CDK2-HA (C177S)	29	2	CDK2-C177S-HA	integration into single FRT site, electroporation	this study
----	---------------------------------	----	---	---------------	---	------------

NA=not applicable

Supplemental Table 2. Plasmids, related to STAR Methods.

No.	Name	Backbone	Insert	Method	Resistance bacteria	Resistance cell line	Source
1	pAAV-Histone3.1-iRFP	pAAV	Histone3.1-iRFP	PCR of iRFP from RRID:Addgene 45465 with primers (5'-acgcGTCGACggtgcaggcggagccgg aggtgcgggtggggctggaggagcagctga aggatccgtcgccaggcagcctgacc-3') and (5'-CCCaaagcttTCActtccatcacgccgatctgcc-3') from 25 and cloning into 3 using Sall and HindIII restriction sites	Ampicillin	NA	this study
2	pcDNA3 mAG-Geminin (1/110)	pcDNA3	mAG-Geminin (1-110)	NA	Ampicillin	Neomycin	PMID 18267078
3	pAAV-H3.1-mTurquoise2	pAAV	H3.1-mTurquoise2	NA	Ampicillin	NA	PMID: 28564611
4	CSII-CDK2 sensor (Venus)	CSII	CDK2 sensor (DHB-Venus)	NA	Ampicillin	NA	PMID 24075009
5	pIRESNeomycin3-Cdk2-sensor (Venus)	pIRESNeo3	CDK2 sensor (DHB-Venus)	Subcloning of DHB-Venus from plasmid 4 into pIRESNeomycin3 using AgeI, HPAI and BamHI restriction sites	Ampicillin	Neomycin	this study
6	CAGGS-NLS-Flag-Cas9-IRES-Puromycin	NA	NLS-Flag-Cas9 (WT nuclease)	NA	Ampicillin	Puromycin	PMID 27216209
7	pIRES2-EGFP	pIRES	EGFP	NA	Kanamycin	Neomycin	Clontech
8	pIRESNeomycin3	pIRESNeo3	empty	NA	Ampicillin	Neomycin	Clontech
9	pIRESNeomycin3-CAGGS promoter	pIRESNeo3	CAGGS promoter	Subcloning of CAGGS promoter from plasmid 6 into 8 using SnaBI and NheI restriction sites	Ampicillin	Neomycin	this study
10	CSII-CDK2 sensor (DHB-mCherry)	CSII	CDK2 sensor (DHB-mCherry)	NA	Ampicillin	NA	PMID 24075009
11	pIRESNeomycin3-CDK2 sensor (DHB-mCherry)	pIRESNeo3	CDK2 sensor (DHB-mCherry)	PCR of DHB-mCherry with primers (5'-Ggaattcaccatgacaaatgatgtcacctgg-3') and (5'-ATAAGAATgcccgccttactgtacagctgctccatgcc-3') from plasmid 10 and cloning into 9 using EcoRI and NotI restriction sites	Ampicillin	Neomycin	this study
12	pIRES-Puromycin3	pIRESPuro3	NA	NA	Ampicillin	Puromycin	Clontech
13	pIRES-Puromycin3	pIRESNeo3	CDK2 sensor	Subcloning of DHB-mCherry from plasmid 11 into 12 using NdeI and NotI restriction sites	Ampicillin	Puromycin	this study

	CDK2 sensor (DHB-mCherry)		(DHB-mCherry)				
14	pLL3.7m-Clover-Geminin(1-110)-IRES-mKO2-Cdt(30-120)	pLL3.7m	Clover-Geminin(1-110)-IRES-mKO2-Cdt(30-120)	NA	Ampicillin	NA	RRID:Add gene_83841
15	pC1-HyPer-3	pC1	HyPer-3	NA	Kanamycin	Neomycin	RRID:Add gene_42131
16	pC1-Clover-Geminin(1-110)-IRES-mKO2-Cdt(30-120)	pC1	Clover-Geminin(1-110)-IRES-mKO2-Cdt(30-120)	Subcloning of Clover-Geminin(1-110)-IRES-mKO2-Cdt(30-120) from plasmid 14 into 15 using NheI and SmaI restriction sites	Kanamycin	Neomycin	this study
17	pC1-Clover-Geminin(1-110)-IRES-Histone3.1-Turquoise2	pC1	Clover-Geminin(1-110)-IRES-Histone3.1-Turquoise2	PCR of Clover-Geminin(1-110)-IRES-Histone3.1-Turquoise2 with primers (5'-CGgaattcATGGCGCGTACTAAGCAGAC-3') and (5'-CGGGATCctcactgtacagctcgccatgc-3') from 3 and cloned into 16 using EcoRI and BamHI restriction sites	Kanamycin	Neomycin	this study
18	pAAV-Hyper2-DAO-NLS	pAAV	Hyper2-DAO-NLS	NA	Ampicillin	NA	PMID 24020354
19	pCS2-HyPer7	pCS2	HyPer7	NA	Ampicillin	NA	PMID 32130885
20	pIRESNeomycin3-CDK2-StrepII-WT	pIRESNeomycin3	CDK2-StrepII-WT	PCR of CDK2-StrepII-WT with primers (5'-ccgCTCGAGATGGAGAACTTCCAAAAGGTGGAAAAG-3') and (5'-cgGGATCCTCATTTCGAACTGCGGGTGGCTCCAGCCAGCGCCGAGTCTGAAGATGGGGTACTGGCTTGGTCACATCC-3') from cDNA and cloning into 8 using XhoI and BamHI restriction sites	Ampicillin	Neomycin	this study
21	pIRESNeomycin3-CDK2-StrepII-C177S	pIRESNeomycin3	CDK2-StrepII-C177S	PCR CDK2-StrepII-C177S with primers (5'-tgttggtaccgagctcctgaaatcctctgggctgcaaataattccacagctgtggacatctggagcctgggcAGcatcttggctgagatgggactcgccgggcc-3') and (5'-cgGGATCCTCATTTCGAACTGCGGGTGGCTCCAGCCAGCGCCGAGTCTGAAGATGGGGTACTGGCTTGGTCACATCC-3') from 20 and cloning into 20 using SacI and BamHI restriction sites	Ampicillin	Neomycin	this study
22	pIRESNeomycin3-CDK2-StrepII-C177A	pIRESNeomycin3	CDK2-StrepII-C177A	PCR of CDK2-StrepII-C177A with primers (5'-tgttggtaccgagctcctgaaatcctctgggctgcaaataattccacagctgtggacatctggagcctgggcGCcatcttggctgagatgggactcgccgggcc-3') and (5'-cgGGATCCTCATTTCGAACTGCGGGTGGCTCCAGCCAGCGCC	Ampicillin	Neomycin	this study

				GAGTCGAAGATGGGGTACTGG CTTGGTCACATCC-3') from 20 and re-cloned into 20 using SacI and BamHI restriction sites			
23	pIRESN eomycin 3-Cdk6- StreptII- WT	pIRESNeo 3	CDK6- StreptII-WT	PCR of CDK6 with primers (5'- ccgCTCGAGATGGAGAAGGACG GCCTGTGCCGCGTGACC-3') and (5'- cgGGATCCTCATTTCGAACTG CGGGTGGCTCCAGCCAGCGCC GGCTGTATTAGCTCCGAGGT GTTCTGGCTGGGCGGCAGG-3') from cDNA and cloning into 8 using XhoI and BamHI restriction sites	Ampicillin	Neomycin	this study
24	pAAV- Hyper2- DAO- NES	pAAV	Hyper2- DAO-NES	NA	Ampicillin	NA	PMID 24020354
25	pMito- iRFP713	pN1	iRFP713	NA	Kanamycin	Neomycin	RRID:Add gene_ 45465
26	pIRES2- CDK2(W T)- IRES2- eGFP	pAAV	CDK2 WT + eGFP	PCR of CDK2 from plasmid 28 with 5'- ccgCTCGAGATGGAGAACTTCC AAAAGGTGGAAAAG-3' and 5'- cgGGATCCtcagagtcgaagatgggta ctgg-3' and cloning into the XhoI and BamHI sites of 7	Ampicillin	Neomycin	this study
27	pIRES2- CDK2(C 177S)- IRES2- mRuby	pN1	CDK2 C177S + mRuby	PCR of CDK2 from plasmid 29 with 5'- ccgCTCGAGATGGAGAACTTCC AAAAGGTGGAAAAG-3' and 5'- cgGGATCCtcagagtcgaagatgggta ctgg-3' cloning into the XhoI and BamHI sites of 7, where eGFP was replaced by mRuby	Kanamycin	Neomycin	this study
28	pDNA5 FRT/TO CDK2(W T)-HA	pCDNA5 FRT/TO neo	CDK2- WT-HA	Subcloning of CDK2 WT from plasmid 30 (NotI and AfeI) into plasmid 32 (NotI and EcoRV)	Ampicillin	Neomycin	this study
29	pIRESN eomycin 3_CDK2 (C177S) -HA	pCDNA5 FRT/TO neomycin resistance	CDK2- C177S-HA	Subcloning of CDK2 C177S from plasmid 31 into plasmid 28 using BsrG1 and NotI	Ampicillin	Neomycin	this study
30	pIRESN eomycin 3_CDK2 (WT)-HA	pIRESNeo 3	CDK2- WT-HA	PCR of CDK2 WT from plasmid 20 with 5'- ccgCTCGAGATGGAGAACTTCC AAAAGGTGGAAAAG-3' and 5'- gcGGATCCtcacgcatagtcaggaacat cgtatgggtaGCCAGCGCCgagtcgaa gatggggtactggctgtgcatcc-3' and cloning into the XhoI and BamHI sites of plasmid 8	Kanamycin	Neomycin	this study
31	pIRESN eomycin 3- CDK2(C 177S)- HA	pIRESNeo 3	CDK2- C177S-HA	PCR of CDK2 C177S from plasmid 21 with 5'- ccgCTCGAGATGGAGAACTTCC AAAAGGTGGAAAAG-3' and 5'- gcGGATCCtcacgcatagtcaggaacat cgtatgggtaGCCAGCGCCgagtcgaa gatggggtactggctgtgcatcc-3' and cloning into the XhoI and BamHI sites of plasmid 8	Kanamycin	Neomycin	this study

NA=not applicable